

# Cosmological Constraints from Weak Lensing Surveys

Dipak Munshi<sup>1,2</sup>, Patrick Valageas<sup>3</sup>

<sup>1</sup>*Institute of Astronomy, Madingley Road, Cambridge, CB3 0HA, United Kingdom*

<sup>2</sup>*Astrophysics Group, Cavendish Laboratory, Madingley Road, Cambridge CB3 0HE, United Kingdom*

<sup>3</sup>*Service de Physique Théorique, CEA Saclay, 91191 Gif-sur-Yvette, France*

5 February 2008

## ABSTRACT

Focusing on the well motivated aperture mass statistics  $M_{\text{ap}}$ , we study the possibility of constraining cosmological parameters using future space based SNAP class weak lensing missions. Using completely analytical results we construct the covariance matrix for estimators based on two-point and three-point statistics. Our approach incorporates an accurate modelling of higher-order statistics to describe cosmic variance as well as various sources of discrete noise at small angular scales. These results are then fed into a Fisher matrix based analysis to study cosmological parameter degeneracies. Joint and independent analysis, with or without redshift binning, for various parameter combinations are presented. An analytical modelling of the covariance matrix opens up the possibility of testing various approximations which are often used in derivations of semi-analytical results. These include how inclusion of full non-Gaussian terms in covariance matrix affects parameter estimation. Inclusion of three-point information and how such information can enhance the accuracy with which certain parameters can be estimated is also studied in detail. It is shown that broad correlation structure among various angular scales in such circumstances mean reduction in number of available angular scales which carry completely independent information. On the other hand, the effect of theoretical inaccuracies, in modelling either the power-spectrum or bi-spectrum evolution, onto the measure of cosmological parameters from weak lensing surveys is also considered. Several cosmological parameters,  $\Omega_m$ ,  $\sigma_8$ , spectral index  $n_s$ , running of spectral index  $\alpha_s$  and equation of state of the dark energy  $w_{\text{de}}$  are included in the analysis.

**Key words:** Cosmology: theory – gravitational lensing – large-scale structure of Universe – Methods: analytical, statistical, numerical

## 1 INTRODUCTION

Weak lensing surveys are expected to make significant contribution in constraining cosmology by studying the statistics of dark matter distribution in the nearby universe in an unbiased way. For instance, Contaldi et al.(2003) used the Red Cluster Sequence (RCS) to show that the  $\Omega_m$  and  $\sigma_8$  degeneracy directions are nearly orthogonal making them particularly suitable for combined analysis (van Waerbeke et al. 2002). Ishak et al. (2003) argued that joint CMB-cosmic shear surveys provide an optimal data set for constraining the amplitude and running of spectral index which helps to probe various inflationary models. Tereno et. al.(2004) have studied cosmological forecasts for joint CMB and weak lensing survey data. Clearly, the potential of weak lensing surveys (Mellier 1999; Bartelmann & Schneider 2001; Réfrégier 2003; van Waerbeke & Mellier 2003) as a cosmological probe is now well established (Contaldi et al. 2003; Hu & Tegmark

1999). In last few years there have been many studies which have directly detected cosmological shear in random patches of the sky (Brown et al. 2003; Bacon et al. 2002; Bacon, Refregier & Ellis 2000; Hamana et al. 2003; Hämmerle et al. 2002; Hoekstra et al. 2002a; Hoekstra, Yee & Gladders 2002a; Jarvis et al. 2002; Kaiser, Wilson & Luppino 2000; Maoli et al. 2001; Refregier, Rhodes, & Groth 2002; Rhodes, Refregier & Groth 2001; van Waerbeke et al. 2000; van Waerbeke et al. 2001a; van Waerbeke et al. 2002; Wittman et al. 2000). While early studies were primarily concerned with detection of weak lensing signal, present generation of weak lensing studies are putting constraints on cosmological parameters such as matter density parameter  $\Omega_m$  and power spectrum normalisation  $\sigma_8$ . Not only these studies can put remarkable constraints on cosmological parameters, they can help to break up parameter degeneracies when used along with other cosmological surveys such as CMB observations as we discussed above.

Inspired by the success of these surveys, there are many other ongoing, planned and proposed weak lensing surveys which are currently in progress such as the Deep Lens Survey (Wittman et al. 2002), the NOAO Deep survey (Mellier et al. 2001)<sup>1</sup>, the Canada-France-Hawaii Telescope Legacy Survey (Mellier et al. 2001)<sup>2</sup>, the Panoramic Survey Telescope and Rapid Response System<sup>3</sup>, the Supernova Acceleration Probe<sup>4</sup> (Rhode et al. 2003; Massey et al. 2003) and the large Synoptic Survey Telescope<sup>5</sup> (Tyson et al. 2002). Independently or jointly these observations can contribute to increase the accuracy with which various cosmological parameters can be determined from other cosmological observations such as CMB. While first generations of cosmic shear surveys have demonstrated (van Waerbeke & Mellier 2003; Refregier 2003) the feasibility of weak lensing studies in constraining the dark matter power spectrum parametrised by  $\sigma_8$ ,  $\Omega_m$  and shape parameter  $\Gamma$  (Munshi & Valageas 2005 contains a recent compilation of present ground based survey results), the future surveys will be able to probe much larger scales and therefore it will be possible to study the linear regime directly to put more stringent bounds on cosmological parameters such as the equation of state of dark energy and its time variations.

Various groups have carried out detailed analysis of cosmological constraints that are achievable from ground and space based weak lensing surveys (Bernardeau et al. 1997, Jain & Seljak 1997, Kaiser 1998). Early studies focused mainly on a limited number of cosmological parameters whereas later on it was realised that weak lensing can play an important role in constraining the dark energy equation of state (Hu 1999, 2002ab; Hueter 2002; Abazajian & Dodelson 2003; Heavens 2003; Refregier et al. 2003; Benabed & van Waerbeke 2003; Jain & Taylor 2003 and references therein). Hu & Tegmark (2004) studied a general multi-parameter Fisher matrix analysis based on power spectrum to check prospects of weak lensing for parameter estimation independently or jointly with external data set such as CMB. Takada & Jain (2005) have presented a study based on joint analysis of power spectrum and bi-spectrum and emphasised the role of tomography in weak lensing parameter estimation. More recently Kilbinger & Schneider (2005) have studied joint constraints from second- and third- order moments based on aperture mass  $M_{ap}$  statistics to study cosmological parameter estimation efficiency. Although similar in motivation we use a different analytical approach to check the efficiency of future space based weak lensing surveys to constrain cosmology. We combine measurements from second  $\langle M_{ap}^2 \rangle$  and third order  $\langle M_{ap}^3 \rangle$  statistics to constrain cosmological parameters such as  $\Omega_m$ ,  $\sigma_8$ ,  $\alpha_s$ ,  $n_s$  and  $w_{de}$ . The effect of estimating the median redshift  $z_0$  of the source redshift distribution directly from the data is also included. Impact of inaccurate modelling of power-spectrum and bi-spectrum of the underlying mass distribution is also analysed.

The reasons for choosing  $M_{ap}$  over other two-point statistics, as pointed out by Kilbinger & Schneider (2005),

are several. Unlike other two-point statistics  $M_{ap}$  by construction is a scalar object and unlike many other three-point objects, constructed from shear three-point correlation functions, the third order moment of  $M_{ap}$  has a non-vanishing ensemble average and hence can directly probe the underlying bi-spectrum of the matter distribution. Besides,  $M_{ap}$  and its extensions has the inherent characteristic of separating gravity induced  $E$  mode from  $B$  mode (see e.g. Crittenden et al. 2001, for more detailed discussion on this issue) generated mainly by residual systematics which can affect both second- and third-order estimators. Moreover, it is to be noted that the integral measure  $\langle M_{ap}^3 \rangle$  is also a local measure of the bi-spectrum and does not suffer from the oscillatory nature of other filters.

This paper is organised as follows. In section 2 we introduce the second- and third- order estimators based on  $M_{ap}$  statistics. Expressions are presented for their joint covariances. Section 3 describes the cosmological parameters and the survey design for proposed SNAP class experiments. Next, in sections 4 and 5 we study the influence of non-Gaussianities onto the covariance matrices and the signal to noise ratios. In section 6 we introduce the Fisher matrix formalism in our context and use it to study estimation error for weak lensing observable. Finally the section 5 is left for discussion of our results and future prospects. Appendix A is devoted to comparing the performance of ground based surveys and SNAP class space based surveys. It also takes a detailed look at various issues of weak lensing survey design.

## 2 APERTURE-MASS STATISTICS

### 2.1 Weak-lensing effects

Weak gravitational lensing effects probe the matter distribution integrated along the line of sight to distant sources like galaxies (e.g., Bernardeau et al. 1997; Kaiser 1998). Therefore, they can be used to obtain information on the 2-D projected density field  $\kappa$  (also called the convergence field) on the sky. In practice, one needs to take into account the redshift distribution  $n(z_s)$  of the sources. Indeed, in order to have good statistics one needs to average weak lensing effects over many sources which entails rather broad source distributions. On the other hand, it can be convenient to use a filtered version of the convergence  $\kappa$ , such as the aperture-mass  $M_{ap}$ . More specifically, the latter is obtained from  $\kappa$  by using a compensated filter. Then, one can also express  $M_{ap}$  as a function of the tangential shear  $\gamma_t$  (Kaiser 1994; Schneider 1996) which can be directly estimated from the observed ellipticities of distant galaxies. This is the property which makes the aperture-mass a useful quantity. In addition, since it involves a compensated filter the contribution from long wavelengths to the signal is damped as compared with a top-hat filter (which would yield the mean convergence) so that  $M_{ap}$  allows one to probe the matter density field over a narrow range of wavelengths which can be varied through the angular scale  $\theta_s$  of the window  $U_{M_{ap}}(\vec{\theta})$ . Thus, the aperture-mass can be written in terms of the fluctuations of the density field as:

$$M_{ap} = \int d\vec{\theta} U_{M_{ap}}(\vec{\theta}) \int_0^{\chi_{max}} d\chi \tilde{w}(\chi) \delta(\chi, \mathcal{D}\vec{\theta}), \quad (1)$$

with:

<sup>1</sup> <http://www.noao.edu/noao/noaodeep/>

<sup>2</sup> <http://www.cfht.hawaii.edu/Science/CFHLS/>

<sup>3</sup> <http://pan-starrs.ifa.hawaii.edu/public/>

<sup>4</sup> <http://snap.lbl.gov/>

<sup>5</sup> <http://www.lsst.org/>

$$\tilde{w}(\chi) = \frac{3\Omega_m}{2} \int_z^{z_{\max}} dz_s n(z_s) \frac{H_0^2}{c^2} \frac{\mathcal{D}(\chi)\mathcal{D}(\chi_s - \chi)}{\mathcal{D}(\chi_s)} (1+z). \quad (2)$$

Here the redshift  $z$  corresponds to the radial distance  $\chi$  and  $\mathcal{D}$  is the angular distance,  $\vec{\vartheta}$  is the angular direction on the sky,  $\delta(\chi, \mathcal{D}\vec{\vartheta})$  is the matter density contrast and hereafter we normalise the mean redshift distribution of the sources (e.g. galaxies) to unity:  $\int dz_s n(z_s) = 1$ . We defined  $z_{\max}$  as the depth of the survey (i.e.  $n(z_s) = 0$  for  $z_s > z_{\max}$ ). Here and in the following we use the Born approximation which is well-suited to weak-lensing studies: the fluctuations of the gravitational potential are computed along the unperturbed trajectory of the photon (Kaiser 1992). We also neglect the discrete effects due to the finite number of galaxies. They can be obtained by taking into account the discrete nature of the distribution  $n(z_s)$ . This gives corrections of order  $1/N$  to higher-order moments of weak-lensing observable, where  $N$  is the number of galaxies within the circular field of interest. In practice  $N$  is much larger than unity (for a circular window of radius 1 arcmin we expect  $N \gtrsim 100$  for the SNAP mission) therefore in this paper we shall work with eq.(1). We choose for the filter  $U_{M_{\text{ap}}}$  associated with the aperture-mass  $M_{\text{ap}}$  the window of finite support used in Schneider (1996):

$$U_{M_{\text{ap}}} = \frac{\Theta(\vartheta < \theta_s)}{\pi\theta_s^2} 9 \left(1 - \frac{\vartheta^2}{\theta_s^2}\right) \left(\frac{1}{3} - \frac{\vartheta^2}{\theta_s^2}\right), \quad (3)$$

where  $\Theta$  is a top-hat with obvious notations. The angular radius  $\theta_s$  gives the angular scale probed by this smoothed observable. As described in Munshi et al. (2004), the cumulants of  $M_{\text{ap}}$  can be written in Fourier space as:

$$\begin{aligned} \langle M_{\text{ap}}^p \rangle_c &= \int_0^{\chi_{\max}} \prod_{i=1}^p d\chi_i \tilde{w}(\chi_i) \int \prod_{j=1}^p d\mathbf{k}_j W_{M_{\text{ap}}}(\mathbf{k}_{\perp j} \mathcal{D}_j \theta_s) \\ &\times \left( \prod_{l=1}^p e^{i\mathbf{k}_{\parallel l} \chi_l} \right) \langle \delta(\mathbf{k}_1) \dots \delta(\mathbf{k}_p) \rangle_c. \end{aligned} \quad (4)$$

We note  $\langle \dots \rangle$  the average over different realizations of the density field,  $k_{\parallel}$  is the component of  $\mathbf{k}$  parallel to the line-of-sight,  $\mathbf{k}_{\perp}$  is the two-dimensional vector formed by the components of  $\mathbf{k}$  perpendicular to the line-of-sight and  $W_{M_{\text{ap}}}(\mathbf{k}_{\perp} \mathcal{D} \theta_s)$  is the Fourier transform of the window  $U_{M_{\text{ap}}}$ :

$$W_{M_{\text{ap}}}(\mathbf{k}_{\perp} \mathcal{D} \theta_s) = \int d\vec{\vartheta} U_{M_{\text{ap}}}(\vec{\vartheta}) e^{i\mathbf{k}_{\perp} \cdot \mathcal{D} \vec{\vartheta}} = \frac{24J_4(k_{\perp} \mathcal{D} \theta_s)}{(k_{\perp} \mathcal{D} \theta_s)^2}. \quad (5)$$

The Fourier-space expression (4) is well suited to models which give a simple expression for the correlations  $\langle \delta(\mathbf{k}_1) \dots \delta(\mathbf{k}_p) \rangle_c$ , such as the stellar model (Valageas et al. 2004; Barber et al. 2004) defined by:

$$\langle \delta(\mathbf{k}_1) \dots \delta(\mathbf{k}_p) \rangle_c = \frac{\tilde{S}_p}{p} \delta_D(\mathbf{k}_1 + \dots + \mathbf{k}_p) \sum_{i=1}^p \prod_{j \neq i} P(k_j), \quad (6)$$

where  $\tilde{S}_2 = 1$ ,  $\delta_D$  is the Dirac distribution and  $P(k)$  is the 3-D power-spectrum of the density fluctuations. The coefficients  $\tilde{S}_3, \tilde{S}_4, \dots$  are closely related (and approximately equal) to the skewness, kurtosis, ..., of the density field. Eq.(4) generalises in a straightforward fashion for many-point cumulants. This allows one to consider for instance the cross-correlations between the two statistics  $M_{\text{ap}1}$  and  $M_{\text{ap}2}$  associated with two different angular scales  $\theta_{s1}, \theta_{s2}$  and/or two different redshift distributions  $n_1(z_s), n_2(z_s)$ .

## 2.2 Low-order estimators

The expressions recalled in the previous section describe weak lensing effects due to the fluctuations of the matter density field. In practice, one actually measures the aperture-mass  $M_{\text{ap}}$  from the distortions of the images of distant sources. Thus, in the case of weak lensing ( $|\kappa| \ll 1$ ) the observed complex ellipticity  $\epsilon = \epsilon_1 + i\epsilon_2$  of a distant galaxy is related to the shear  $\gamma = \gamma_1 + i\gamma_2$  by:  $\epsilon = \gamma + \epsilon_*$ , where  $\epsilon_*$  is the intrinsic ellipticity of the galaxy. On the other hand, the aperture-mass defined in eqs.(1)-(3) can also be written as a function of the tangential shear  $\gamma_t$  as (Kaiser et al. 1994, Schneider 1996) as:

$$M_{\text{ap}} = \int d\vec{\vartheta} Q_{M_{\text{ap}}}(\vec{\vartheta}) \gamma_t(\vec{\vartheta}) \quad (7)$$

with:

$$Q_{M_{\text{ap}}}(\vec{\vartheta}) = \frac{\Theta(\vartheta < \theta_s)}{\pi\theta_s^2} 6 \left(\frac{\vartheta}{\theta_s}\right)^2 \left(1 - \frac{\vartheta^2}{\theta_s^2}\right). \quad (8)$$

This leads us to define the estimators  $M_p$  for low-order moments (e.g., Munshi & Coles 2003, Valageas et al. 2004b):

$$M_p = \frac{(\pi\theta_s^2)^p}{(N)^p} \sum_{(j_1, \dots, j_p)}^N Q_{j_1} \dots Q_{j_p} \epsilon_{tj_1} \dots \epsilon_{tj_p}, \quad (9)$$

with:

$$(N)_p = N(N-1) \dots (N-p+1) = \frac{N!}{(N-p)!}, \quad (10)$$

where  $N$  is the number of galaxies in the patch of size  $\pi\theta_s^2$ ,  $p$  is the order of the moment and  $Q_j = Q_{M_{\text{ap}}}(\vec{\vartheta}_j)$  where  $\vec{\vartheta}_j$  and  $\epsilon_{tj}$  are the direction on the sky and the observed tangential ellipticity of the galaxy  $j$ . Finally, the sum in eq.(9) runs over all sets of  $p$  different galaxies among the  $N$  galaxies enclosed in the angular radius  $\theta_s$ , which ensures that  $\langle M_p \rangle = \langle M_{\text{ap}}^p \rangle$  if we neglect the correlation of the intrinsic ellipticity of a given galaxy with other galaxies or with weak lensing observables.

These estimators  $M_p$  correspond to a single circular field of angular radius  $\theta_s$  containing  $N$  galaxies. In practice, the size of the survey is much larger than  $\theta_s$  and we can average over  $N_c$  cells on the sky. This yields the estimators  $\mathcal{M}_p$  defined by:

$$\mathcal{M}_p = \frac{1}{N_c} \sum_{n=1}^{N_c} M_p^{(n)}, \quad \text{whence} \quad \langle \mathcal{M}_p \rangle = \langle M_{\text{ap}}^p \rangle, \quad (11)$$

where  $M_p^{(n)}$  is the estimator  $M_p$  for the cell  $n$  and we assumed that these cells are sufficiently well separated so as to be uncorrelated. The estimators  $M_p$  and  $\mathcal{M}_p$  provide a measure of the moments  $\langle M_{\text{ap}}^p \rangle$ , which can be used to constrain cosmological parameters. However, as shown in Valageas et al. (2004b), it is better to first consider cumulant-inspired estimators  $H_p$ . Thus, for the second and third-order cumulants we define:

$$H_2 = M_2, \quad H_3 = M_3 - 3\mathcal{M}_2 M_1, \quad (12)$$

and:

$$\mathcal{H}_p = \frac{1}{N_c} \sum_{n=1}^{N_c} H_p^{(n)}, \quad \langle \mathcal{H}_2 \rangle = \langle M_{\text{ap}}^2 \rangle_c, \quad \langle \mathcal{H}_3 \rangle = \langle M_{\text{ap}}^3 \rangle_c. \quad (13)$$

The interest of  $\mathcal{H}_3$  is that its scatter is smaller than for  $\mathcal{M}_3$ , see Valageas et al.(2004b). Besides it directly yields the one-point cumulants (here we neglected higher-order terms over  $1/N_c$ ).

### 2.3 Covariance matrix

The estimators  $\mathcal{M}_p$  and  $\mathcal{H}_p$  defined in the previous section allow one to estimate the cumulants of the aperture-mass  $\langle M_{\text{ap}}^p \rangle_c$  for a given angular scale  $\theta_s$  and source redshift distribution  $n(z_s)$ . In practice we can vary both the angular scale  $\theta_s$  of the filters  $U_{M_{\text{ap}}}$  and  $Q_{M_{\text{ap}}}$  and the redshift distribution  $n(z_s)$  (for instance by applying a simple binning of the galaxies over redshift and selecting different redshift bins, which is often referred to as tomography). Thus, if we restrict ourselves to second-order moments  $\langle M_{\text{ap}}^2 \rangle$  we obtain the set of estimators  $\mathcal{H}_2(i)$ , with  $\langle \mathcal{H}_2(i) \rangle = \langle M_{\text{ap}}^2(i) \rangle$  as defined in eq.(13), where the index  $i = 1, \dots, N_i$  stands for both the angular scale  $\theta_{si}$  and the redshift distribution  $n_i(z_s)$  (for  $N_\theta$  angular scales and  $N_z$  redshift bins we have  $N_i = N_\theta \times N_z$ ). Then, the covariance matrix  $C_{ij}$  associated with this data set is:

$$C_{ij} = \langle \mathcal{H}_2(i) \mathcal{H}_2(j) \rangle - \langle \mathcal{H}_2(i) \rangle \langle \mathcal{H}_2(j) \rangle. \quad (14)$$

It measures the cross-correlation between the two estimators  $\mathcal{H}_2(i)$  and  $\mathcal{H}_2(j)$ . In the following, we shall consider the limit where the number of cells  $N_c$  on the sky goes to infinity, that is the sum in eq.(13) is performed over  $N_c$  cells which cover the whole survey area with a uniform coverage and which are separated by an angular shift  $\Delta\vec{\alpha}$  which goes to zero. Therefore, the discrete sum (13) tends to the integral:

$$\mathcal{H}_2(i) = \int_A \frac{d\vec{\alpha}}{A} H_2(i; \vec{\alpha}), \quad (15)$$

where  $A$  is the survey area and  $H_2(i; \vec{\alpha})$  is the estimator  $H_2(i)$ , associated with the angular scale  $\theta_{si}$  and redshift distribution  $n_i(z_s)$ , for the cell centred on the direction  $\vec{\alpha}$  on the sky. Hereafter we neglect side effects and we consider that all estimators cover the same area  $A$ , independently of the radius  $\theta_{si}$ . Then, after one angular integration we obtain for the covariance  $C_{ij}$ :

$$C_{ij} = \int_A \frac{d\vec{\alpha}}{A} \sigma^2(H_2(i), H_2(j); \vec{\alpha}), \quad (16)$$

where  $\sigma^2(H_2(i), H_2(j); \vec{\alpha})$  is the cross-correlation between the two estimators  $H_2(i)$  and  $H_2(j)$  separated by the angular shift  $\vec{\alpha}$ . From eq.(9) the cross-correlation  $\sigma^2$  reads (see also the expressions given in App.A1 of Munshi & Valageas 2005):

$$\sigma^2(H_2(i), H_2(j); \vec{\alpha}) = \langle M_{\text{ap}}^2(i) M_{\text{ap}}^2(j) \rangle_c(\vec{\alpha}) + 2[\langle M_{\text{ap}}(i) M_{\text{ap}}(j) \rangle_c(\vec{\alpha}) + Q_{ij}(\vec{\alpha})]^2, \quad (17)$$

where we recalled explicitly the dependence on the angular shift  $\vec{\alpha}$ , and we introduced  $Q_{ij}$  defined by:

$$Q_{ij}(\vec{\alpha}) = \frac{\sigma_*^2}{2} \frac{n_{gi}}{n_{gi} n_{gj}} \int d\vec{\vartheta} Q_i(\vec{\vartheta}) Q_j(\vec{\vartheta} - \vec{\alpha}), \quad (18)$$

where  $\sigma_*^2 = \langle |\epsilon_*|^2 \rangle$  is the scatter of the galaxy intrinsic ellipticities,  $n_{gi}$  is the number surface density of galaxies associated with the redshift distribution  $n_i(z_s)$ ,  $n_{gj}$  is the surface density of common galaxies to both redshift distributions

$n_i(z_s)$  and  $n_j(z_s)$ , and  $Q_i$  is the filter  $Q_{M_{\text{ap}}}$  defined in eq.(8) for the radius  $\theta_{si}$ . We can obtain in a similar fashion the covariance matrix associated with the data set  $\{\mathcal{H}_3(i)\}$ , associated with third-order cumulants, as well as the full data set  $\{\mathcal{H}_2(i), \mathcal{H}_3(i)\}$  where we consider both second-order and third-order cumulants. Thus, we have (see also Munshi & Valageas 2005):

$$\sigma^2(H_2(i), H_3(j)) = \langle M_{\text{ap}}^2(i) M_{\text{ap}}^3(j) \rangle_c + 6\langle M_{\text{ap}}(i) M_{\text{ap}}^2(j) \rangle_c [\langle M_{\text{ap}}(i) M_{\text{ap}}(j) \rangle_c + Q_{ij}], \quad (19)$$

and:

$$\sigma^2(H_3(i), H_3(j)) = \langle M_{\text{ap}}^3(i) M_{\text{ap}}^3(j) \rangle_c + 9\langle M_{\text{ap}}^2(i) M_{\text{ap}}^2(j) \rangle_c [\langle M_{\text{ap}}(i) M_{\text{ap}}(j) \rangle_c + Q_{ij}] + 9\langle M_{\text{ap}}^2(i) M_{\text{ap}}(j) \rangle_c \langle M_{\text{ap}}(i) M_{\text{ap}}^2(j) \rangle_c + 6[\langle M_{\text{ap}}(i) M_{\text{ap}}(j) \rangle_c + Q_{ij}]^3, \quad (20)$$

where we did not recall explicitly the dependence on the angular shift  $\vec{\alpha}$ .

It is interesting to estimate the amplitude of various contributions to the covariance matrix  $C_{ij}$ , due to noise, Gaussian and non-Gaussian terms. Thus, in addition to the full matrix  $C_{ij}$  described above we also introduce the matrices  $C_{ij}^{G,c.v.}$ ,  $C_{ij}^{G,s.n.}$  and  $C_{ij}^{c.v.}$ . The matrix  $C_{ij}^{G,c.v.}$  only includes Gaussian terms which contribute to the cosmic variance (i.e. non-Gaussianities and the noise are set to zero). This yields for instance for  $\sigma^2(H_2(i), H_2(j))^{G,c.v.}$ :

$$\sigma^2(H_2(i), H_2(j))^{G,c.v.} = 2\langle M_{\text{ap}}(i) M_{\text{ap}}(j) \rangle_c^2. \quad (21)$$

We obtain from eq.(20) a similar expression for  $\sigma^2(H_3(i), H_3(j))^{G,c.v.}$ , while from eq.(19) we see at once that  $\sigma^2(H_2(i), H_3(j))^{G,c.v.} = 0$ . Next, the matrix  $C_{ij}^{G,s.n.}$  includes all Gaussian terms which involve the shot noise. This yields for  $\sigma^2(H_2(i), H_2(j))^{G,s.n.}$ :

$$\sigma^2(H_2(i), H_2(j))^{G,s.n.} = 4\langle M_{\text{ap}}(i) M_{\text{ap}}(j) \rangle_c Q_{ij} + 2Q_{ij}^2. \quad (22)$$

We again obtain from eq.(20) a similar relation for  $\sigma^2(H_3(i), H_3(j))^{G,s.n.}$ , while from eq.(19) we see at once that  $\sigma^2(H_2(i), H_3(j))^{G,s.n.} = 0$ . Note that  $C_{ij}^{G,c.v.} + C_{ij}^{G,s.n.}$  is equal to the matrix  $C_{ij}$  without non-Gaussian terms. Finally, the matrix  $C_{ij}^{c.v.}$  is equal to the matrix  $C_{ij}$  where we set the noise equal to zero. It includes both Gaussian and non-Gaussian terms, and we obtain for  $\sigma^2(H_2(i), H_2(j))^{c.v.}$ :

$$\sigma^2(H_2(i), H_2(j))^{c.v.} = \langle M_{\text{ap}}^2(i) M_{\text{ap}}^2(j) \rangle_c + 2\langle M_{\text{ap}}(i) M_{\text{ap}}(j) \rangle_c^2. \quad (23)$$

From eqs.(19)-(20) we obtain similar expressions for  $\sigma^2(H_2(i), H_3(j))^{c.v.}$  and  $\sigma^2(H_3(i), H_3(j))^{c.v.}$ . Note that  $\sigma^2(H_2(i), H_3(j))^{c.v.}$  is different from zero. Thus, the comparison between the four matrices  $C_{ij}$ ,  $C_{ij}^{G,c.v.}$ ,  $C_{ij}^{G,s.n.}$  and  $C_{ij}^{c.v.}$  allows us to evaluate the relative importance of the shot noise (associated with the dispersion  $\sigma_*^2$  of the galaxy intrinsic ellipticity) and of the cosmic variance (merely due to the finite size of the survey), as well as the relative importance of Gaussian and non-Gaussian terms.

## 3 BACKGROUND COSMOLOGY AND SURVEY PARAMETERS

We describe in this section the background cosmology and the specific correlation hierarchy for the matter distribution which we use in numerical computations. We also focus

on the SNAP observational strategy to estimate the accuracy which can be obtained from such weak lensing surveys. However, as mentioned before the basic formalism developed here remains completely general and specific details studied here only serve illustrational purposes.

### 3.1 Cosmological parameters

For the background cosmology we consider a fiducial  $\Lambda$ CDM model with  $\Omega_m = 0.3$ ,  $\Omega_{de} = 0.7$ ,  $w_{de} = -1$ ,  $H_0 = 70$  km/s/Mpc and  $\sigma_8 = 0.88$ . We note  $\Omega_m$  the matter density (cold dark matter plus baryons) and  $\Omega_{de}$  the dark-energy density today at  $z = 0$ . We parameterize its equation of state by  $w_{de} = p_{de}/\rho_{de}$ . For  $w_{de} = -1$  this corresponds to a simple cosmological constant. In the following we shall investigate the dependence of weak-lensing observable on the cosmological parameters  $\Omega_m$  (keeping  $\Omega_m + \Omega_{de} = 1$  for a flat universe) and  $w_{de}$ . We always consider  $w_{de}$  to be a constant independent of time. Then, the Hubble expansion rate  $H(z)$  reads (e.g., Linder & Jenkins 2003):

$$\frac{\dot{a}}{a} = H(z) = H_0 \sqrt{\Omega_m(1+z)^3 + \Omega_{de}(1+z)^{3(1+w_{de})}}, \quad (24)$$

where  $a(t) = (1+z)^{-1}$  is the cosmological scale factor while the dot denotes the derivative with respect to physical time (we used  $\Omega_m + \Omega_{de} = 1$ ). The linear growth factor  $D(t)$  obeys the differential equation:

$$\ddot{D} + 2H\dot{D} - \frac{3}{2}\Omega_m H_0^2(1+z)^3 D = 0, \quad (25)$$

which yields for the linear growth rate  $g(a)$  relative to a critical-density universe  $g = D/a$ :

$$2\frac{d^2g}{d\ln a^2} + \frac{5\Omega_m + (5 - 3w_{de})\Omega_{de}a^{-3w_{de}}}{\Omega_m + \Omega_{de}a^{-3w_{de}}} \frac{dg}{d\ln a} + \frac{(3 - 3w_{de})\Omega_{de}a^{-3w_{de}}}{\Omega_m + \Omega_{de}a^{-3w_{de}}} g = 0. \quad (26)$$

We obtain  $g(a)$  by solving numerically the differential eq.(26).

For the matter transfer function  $T(k)$  we use the fitting formulae provided by Eisenstein & Hu (1999), with  $\Omega_b = 0.047$ ,  $n_s = 1$  and  $\alpha_s = 0$ . Here  $n_s$  is the power-law index of the primordial power-spectrum and  $\alpha_s$  is the running index. More precisely, we write the linear matter power-spectrum as in Spergel et al. (2003):

$$P_L(k) \propto \left(\frac{k}{k_0}\right)^{n_s + \alpha_s \ln(k/k_0)/2} T^2(k), \quad (27)$$

where  $k_0 = 0.05$  Mpc $^{-1}$ . Thus, the local slope  $n$  of the primordial spectrum is:

$$n = \frac{d\ln P_{\text{prim}}}{d\ln k} = n_s + \alpha_s \ln\left(\frac{k}{k_0}\right), \quad \frac{dn}{d\ln k} = \alpha_s. \quad (28)$$

Next, we use the fit given by Peacock and Dodds (1996) to model the non-linear evolution of the matter power-spectrum due to gravitational clustering. In order to investigate the sensitivity of weak lensing data on this non-linear extrapolation we introduce an additional parameter  $f_2$ . Thus, we modify eq.(21) of Peacock & Dodds (1996) as:

$$f_{\text{NL}}(x) = x \left[ \frac{1 + B\beta x + [Ax]^{\alpha\beta}}{1 + ([Ax]^{\alpha} g^3(\Omega_m)/[f_2 V x^{1/2}])^{\beta}} \right]^{1/\beta}. \quad (29)$$

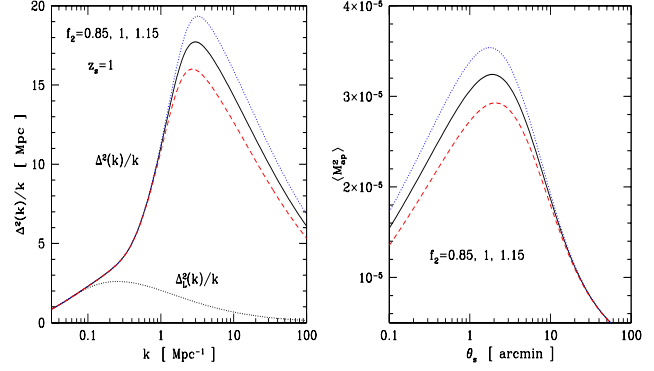


**Figure 1.** *Left panel:* The power  $\Delta^2(k)/k$  at redshift  $z = 1$  as a function of the comoving wavenumber  $k$ . The three upper curves correspond to  $f_2 = 0.85$  (lower dashed curve),  $f_2 = 1$  (middle solid line, this corresponds to Peacock & Dodds 1996) and  $f_2 = 1.15$  (upper dotted curve). This corresponds roughly to a 10% variation of the matter power-spectrum in the highly non-linear regime. The lower dotted curve shows the linear power  $\Delta_L^2(k)/k$ . *Right panel:* The variance  $\langle M_{\text{ap}}^2 \rangle$  of the aperture-mass as a function of smoothing angle  $\theta_s$  for the SNAP survey. We again display the cases  $f_2 = 0.85$  (lower dashed curve),  $f_2 = 1$  (middle solid line) and  $f_2 = 1.15$  (upper dotted curve).

This is identical to the formula from Peacock & Dodds (1996) for  $f_2 = 1$  (see their paper for the meaning of various parameters). In the linear regime we merely have  $f_{\text{NL}}(x) = x$  while in the non-linear regime we have  $f_{\text{NL}}(x) \propto f_2 x^{3/2}$ . Therefore, the parameter  $f_2$  describes the amplitude of the non-linear part of the matter power-spectrum as compared with Peacock & Dodds (1996) (which corresponds to  $f_2 = 1$ ).

For illustration purposes, we show in Fig. 1 the non-linear power  $\Delta^2(k)/k$  (left panel, as a function of comoving wavenumber  $k$ ) at redshift  $z = 1$  and the variance  $\langle M_{\text{ap}}^2 \rangle$  (right panel, as a function of smoothing angle  $\theta_s$ ) for the SNAP survey described in section 3.2 below with no redshift binning. We display the curves obtained for the cases  $f_2 = 0.85, 1, 1.15$  from bottom to top. This corresponds to a variation of about  $\pm 10\%$  for the power-spectrum  $P(k)$  in the non-linear regime. Thus, the range  $f_2 = 1 \pm 0.15$  describes roughly the current uncertainty on the non-linear power-spectrum in the range of interest. Note that  $f_2$  is not merely a multiplicative factor to the non-linear power-spectrum as the recipe from Peacock & Dodds (1996) also involves a rescaling of length scales. Here we defined the 3-D power per logarithmic interval  $\Delta^2(k) = 4\pi k^3 P(k, z)$ . Because of the integration along the line of sight the power relevant for weak lensing observables is actually  $\Delta^2(k)/k$ , and the typical wavenumber associated with the angle  $\theta_s$  is  $k \sim 4/(\mathcal{D}\theta_s)$ , see Munshi et al. (2004). The lower dotted curve in left panel of Fig. 1 shows the linear power  $\Delta_L^2(k)/k$ . We can check that at low wavenumbers and at large angular scales which probe the linear regime the dependence on  $f_2$  disappears.

For higher-order correlations of the matter density field we use the stellar model (6) described in Valageas et al. (2004a). This is actually identical to the minimal tree-model up to third-order moments (Munshi et al. 2004). In particular, for the skewness  $S_3$  of the 3-D matter density field we interpolate between the quasi-linear limit  $S_3^{\text{QL}}$  and the non-

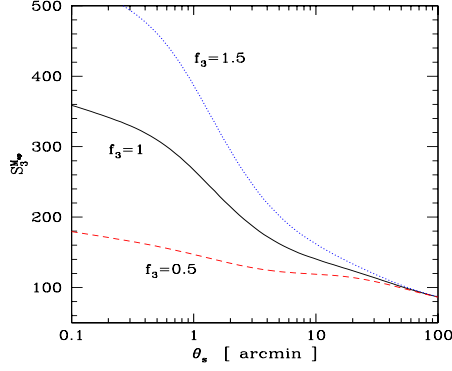


**Figure 2.** The skewness  $S_3^{M_{ap}}$  of the aperture-mass as a function of the smoothing angle  $\theta_s$  for the SNAP survey. We display the cases  $f_3 = 0.5$  (lower dashed curve),  $f_3 = 1$  (middle solid line) and  $f_3 = 1.5$  (upper dotted curve) which correspond to a 50% variation of the skewness in the highly non-linear regime.

linear prediction  $S_3^{\text{HEPT}}$  of HEPT (Scoccimarro et al. 1998). In order to investigate the sensitivity to the non-linear fit used for  $S_3$  we introduce a parameter  $f_3$  and we define the skewness  $S_3^{\text{NL}}$  reached in the highly non-linear regime as:

$$S_3^{\text{NL}} = f_3 S_3^{\text{HEPT}}. \quad (30)$$

Then, on linear scale we use  $S_3 = S_3^{\text{QL}}$  while on highly non-linear scales we use  $S_3 = S_3^{\text{NL}}$ , see Munshi et al. (2004) for details.

We show in Fig. 2 the skewness  $S_3^{M_{ap}} = \langle M_{ap}^3 \rangle / \langle M_{ap}^2 \rangle^2$  as a function of the smoothing angle  $\theta_s$  for the cases  $f_3 = 0.5, 1, 1.5$ , for the SNAP survey described in section 3.2 below with no redshift binning. Thus we now consider a variation of  $\pm 50\%$  on  $f_3$  and  $S_3$  since the skewness is not known to better than 50% in the highly non-linear regime (the actual current uncertainty may actually be even larger). Of course, since the aperture-mass is linear over the density fluctuations within our weak-lensing approximation (1) this yields a 50% variation for  $S_3^{M_{ap}}$  at small angular scales. We can check again that at large angular scales which probe the quasi-linear regime the dependence on  $f_3$  disappears.

Thus, the parameters  $f_2$  and  $f_3$  allow us to evaluate the sensitivity of weak lensing results onto the amplitude of the two-point and three-point matter correlations in the non-linear regime, where they are not known to up to high accuracy yet. Unless otherwise stated, we use  $f_2 = 1$  and  $f_3 = 1$  which correspond to the fits obtained from Peacock & Dodds (1996) and from Scoccimarro et al. (1998).

### 3.2 Survey parameters

Hereafter, we adopt the characteristics of the SNAP mission as given in Refregier et al. (2004). More precisely, we consider the “Wide” survey where the redshift distribution of galaxies is given by:

$$n(z_s) \propto z_s^2 e^{-(z_s/z_0)^2} \quad \text{and} \quad z_0 = 1.13, \quad z_{\text{max}} = 3. \quad (31)$$

The variance in shear due to intrinsic ellipticities and measurement errors is  $\sigma_* = \langle |\epsilon_*|^2 \rangle^{1/2} = 0.31$ . The survey covers an area  $A = 300 \text{ deg}^2$  and the surface density of usable galaxies is  $n_g = 100 \text{ arcmin}^{-2}$ . In order to extract

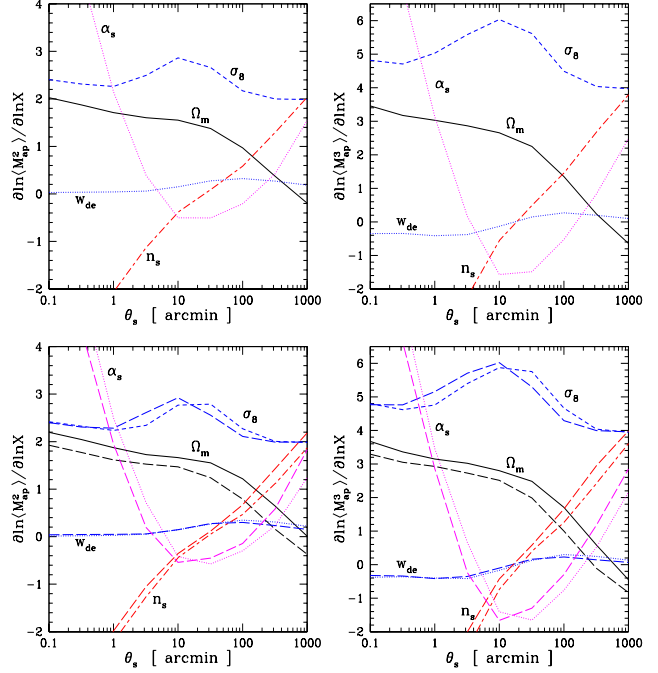


**Figure 3.** The logarithmic derivative  $\partial \ln \langle M_{ap}^p \rangle_c / \partial \ln X$  of low order cumulants with respect to cosmological parameters  $X$ . *Upper left panel:* The dependence of the variance  $\langle M_{ap}^2 \rangle_c$  on  $\Omega_m$  (solid line),  $\sigma_8$  (dashed line),  $w_{de}$  (dotted line),  $n_s$  (dot dashed line) and  $\alpha_s$  (dotted line), as a function of angular scale  $\theta_s$  with no redshift binning. For  $\alpha_s$  we plot  $\partial \ln \langle M_{ap}^2 \rangle_c / \partial \alpha_s$  since  $\alpha_s = 0$  in our fiducial model. *Upper right panel:* Same as upper left panel for the third-order cumulant  $\langle M_{ap}^3 \rangle_c$ . *Lower left panel:* Same as upper left panel but for two redshift bins. The low redshift bin is shown by the same line styles as in upper left panel whereas the high redshift bin is shown by the long dashed line. *Lower right panel:* Same as lower left panel for the third-order cumulant  $\langle M_{ap}^3 \rangle_c$ .

some information from the redshift dependence of weak lensing effects we also divide the “Wide” SNAP survey into two redshift bins:  $0 < z_s < z_*$  and  $z_* < z_s < z_{\text{max}}$ . We choose  $z_* = 1.23$ , which corresponds roughly to the separation provided by the SNAP filters and which splits the “Wide” SNAP survey into two samples with the same number of galaxies (hence  $n_g = 50 \text{ arcmin}^{-2}$ ). Note that one cannot use too many redshift bins at it decreases the number of source galaxies associated with each subsample (for the aperture mass we could still obtain good results with three bins but we shall restrict ourselves to two redshift bins in this paper). The redshift bins that we use are similar to those which were used by Refregier et al. (2003) using photometric redshifts, except that they have a sharp cutoff and non-overlapping source distributions. Note that using overlapping source distributions (over redshift) would increase the cross-correlations.

## 4 DEPENDENCE OF LOW-ORDER ESTIMATORS ON COSMOLOGY

We show in Fig. 3 the logarithmic derivative  $\partial \ln \langle M_{ap}^p \rangle_c / \partial \ln X$  of cumulants of order  $p = 2$  (left panels) and  $p = 3$  (right panels) with respect to cosmo-



logical parameters  $X$ , with no redshift binning (upper panels) and with two redshift bins (lower panels). For the cosmological parameter  $\alpha_s$  we merely plot  $\partial \ln \langle M_{\text{ap}}^p \rangle_c / \partial \alpha_s$  since  $\alpha_s = 0$  in our fiducial model. The rather large values obtained for these derivatives shows that weak lensing effects could potentially constrain cosmological parameters up to a good accuracy. By contrast, the small derivative with respect to  $w_{\text{de}}$  shows that the equation of state of the dark energy component cannot be measured up to a similar accuracy. As expected, since weak lensing effects are proportional to matter density fluctuations, eq.(1), the derivatives with respect to  $\Omega_m$  and  $\sigma_8$  are positive over most of the angular range  $0.1' - 1000'$ . In particular, we can check that  $\langle M_{\text{ap}}^2 \rangle_c \sim \sigma_8^2$  as expected from eq.(1). On the other hand, we can check that  $\partial \langle M_{\text{ap}}^2 \rangle_c / \partial n_s > 0$  at small scales which probe high wavenumbers  $k$  and it crosses zero at about  $20'$  which corresponds to the normalisation of the power-spectrum. Since these derivatives show different variations with the angular scale  $\theta_s$  for different cosmological parameters, one should be able to constrain simultaneously these parameters by using several angular scales. Note that by looking over such a large range of angular scales one can discriminate the behaviours of different cosmological parameters which helps to remove degeneracies. On the other hand, one can use the additional information provided by higher-order cumulants, such as the third-order cumulant (whence the skewness) shown in the right panels. However, we can see that for most parameters  $\langle M_{\text{ap}}^3 \rangle_c$  behaves roughly as  $\langle M_{\text{ap}}^2 \rangle_c^2$ , except for  $\Omega_m$  where there is a residual dependence which can be used to measure for instance both  $\Omega_m$  and  $\sigma_8$  (see also Bernardeau et al. 1997, as well as Kilbinger & Schneider 2005). Alternatively, one can split the survey into two redshift bins and take advantage of the different dependence on cosmology of weak lensing effects associated with each bin. This is shown in both lower panels. Although the curves are quite similar we shall check in sect. 6 that using such a redshift binning does indeed improve the constraints on cosmological parameters.

## 5 COVARIANCE MATRICES OF LOW-ORDER ESTIMATORS

In order to use the estimators  $\mathcal{H}_p$  to measure cosmological parameters, through their dependence on cosmology displayed in Fig. 3, we need the covariance matrices  $C_{ij}$  introduced in sect. 2.3. The latter are necessary to obtain the relevant error bars through a Fisher matrix analysis (sect. 6.1) or a  $\chi^2$  likelihood function (sect. 6.3).

### 5.1 Impact of noise and non-Gaussianities

We first show in Fig. 4 the covariance matrix  $C_{ij}$  of the estimator  $\mathcal{H}_2(\theta_s)$  of the variance  $\langle M_{\text{ap}}^2 \rangle$ , see eqs.(13)-(14), along the diagonal  $i = j$  with no redshift binning ( $\theta_{si} = \theta_{sj}$ ). The full solid line shows the full covariance  $C$  while other line styles correspond to the specific contributions  $C^{G,s.n.}$ ,  $C^{G,c.v.}$  and  $C^{c.v.}$ , defined in eqs.(21)-(23). As expected, we check that at small angular scales  $\theta_s < 1'$  the covariance  $C$  is dominated by the shot-noise due to the galaxy intrinsic ellipticity dispersion, whereas at large scales  $\theta_s > 2'$  the covariance is dominated by the cosmic variance (i.e. the error

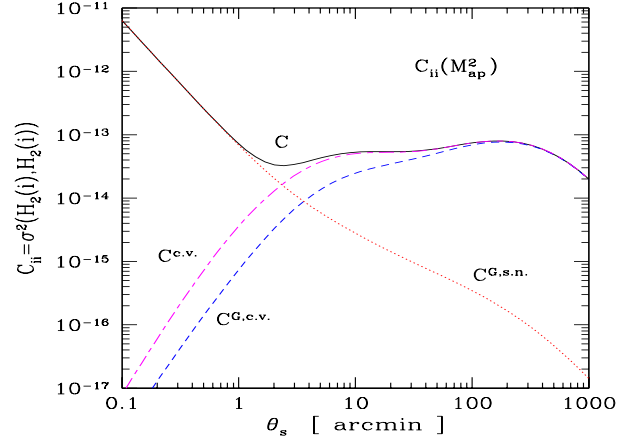


**Figure 4.** Covariance of the estimator  $\mathcal{H}_2(\theta_s)$  of the variance  $\langle M_{\text{ap}}^2 \rangle$ , eqs.(13)-(14). The solid line shows the full covariance  $C_{ii} = \sigma^2(\mathcal{H}_2(\theta_{si}), \mathcal{H}_2(\theta_{si}))$  as a function of smoothing angular scale  $\theta_{si}$ , with no redshift binning. The dotted line displays the contribution  $C^{G,s.n.}$  from the galaxy intrinsic ellipticity dispersion to the Gaussian part of  $C$ . The dashed line  $C^{G,c.v.}$  is the cosmic variance contribution to the Gaussian part of  $C$  while  $C^{c.v.}$  is the cosmic variance contribution to the full matrix  $C$ .

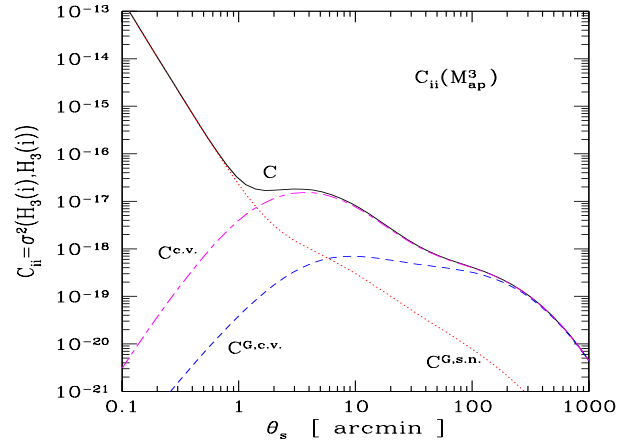


**Figure 5.** Covariance of the estimator  $\mathcal{H}_3(\theta_s)$  of the third-order cumulant  $\langle M_{\text{ap}}^3 \rangle_c$ , eq.(13). The various line styles show different contributions to the full covariance  $C_{ii} = \sigma^2(\mathcal{H}_3(\theta_{si}), \mathcal{H}_3(\theta_{si}))$  (solid line) as in Fig. 4.

bar due to the finite size of the survey). We can also check that the shot noise contribution  $C^{G,s.n.}$  grows as  $1/\theta_s^2$  at smaller scales, which is proportional to the number of distinct patches of radius  $\theta_s$  in the survey. The slow rise of the cosmic variance term  $C^{c.v.}$  yields a broad plateau for the full covariance, from  $1'$  up to  $1000'$ , while non-Gaussianities become negligible above  $30'$ . We can note that even at smallest scales non-Gaussian terms are only twice larger than Gaussian terms so that the Gaussian part  $C^G = C^{G,s.n.} + C^{G,c.v.}$  of the covariance matrix is always a good approximation along the diagonal ( $\theta_{si} = \theta_{sj}$ ) for two-point estimators such as  $\mathcal{H}_2$ .

Next, we display in Fig. 5 the covariance matrix  $C_{ii}$  of the estimator  $\mathcal{H}_3(\theta_s)$  of the third-order cumulant  $\langle M_{\text{ap}}^3 \rangle_c$ , again along the diagonal  $i = j$  with no redshift binning

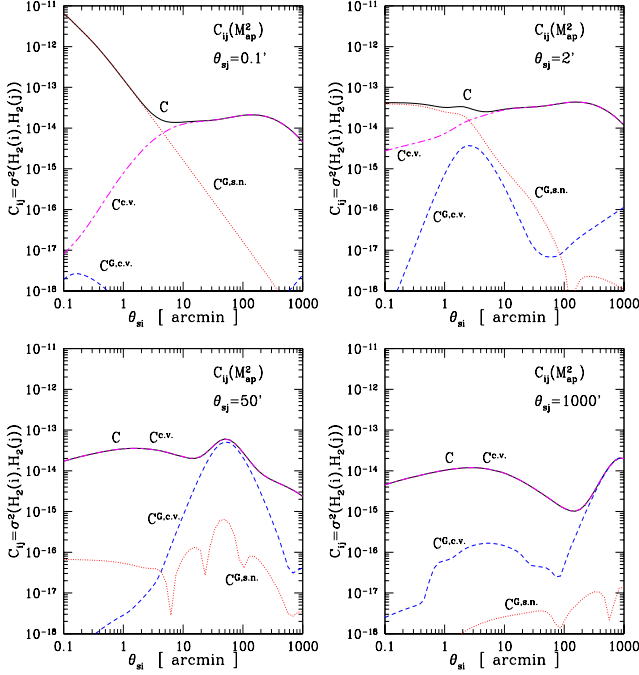


**Figure 6.** Covariance  $C_{ij}$  of the estimator  $\mathcal{H}_2(\theta_s)$  of the variance  $\langle M_{\text{ap}}^2 \rangle$ , eqs.(13)-(14), for different angular scales as a function of  $\theta_{si}$  at fixed  $\theta_{sj}$ , with no redshift binning. The various line styles show different contributions to the full covariance as in Fig. 4. The four panels correspond to  $\theta_{sj} = 0.1'$  (upper left panel),  $\theta_{sj} = 2'$  (upper right panel),  $\theta_{sj} = 50'$  (lower left panel) and  $\theta_{sj} = 1000'$  (lower right panel).

( $\theta_{si} = \theta_{sj}$ ), see eq.(20). We find again that the shot-noise due to the galaxy intrinsic ellipticities dominates below  $2'$ . However, it now grows as  $1/\theta_s^4$  rather than  $1/\theta_s^2$  at smallest scales (this is due to the term  $Q_{ij}^3$  in eq.(20)). Above  $1'$  the covariance is dominated by the cosmic variance but in contrast with Fig. 4 we now find that non-Gaussian terms are larger than Gaussian terms by an order of magnitude around  $\theta_s \sim 3'$  (for the cosmic variance part). This is not really surprising since  $\mathcal{H}_3$  itself is an estimator of non-Gaussianities. However, above  $60'$  non-Gaussianities become negligible again as we probe the quasi-linear regime.

We show in Fig. 6 the covariance  $C_{ij}$  of the estimator  $\mathcal{H}_2(\theta_s)$  of the variance  $\langle M_{\text{ap}}^2 \rangle$  for different angular scales  $\{\theta_{si}, \theta_{sj}\}$  with no redshift binning (i.e. we probe  $C_{ij}$  out of the diagonal whereas Fig. 4 was restricted to the diagonal  $i = j$ ). The line styles are as in Fig. 4. The wiggles in the lower panels for  $C^{G.s.n.}$  correspond to a change of sign (hence we actually plot  $|C^{G.s.n.}|$ ) because at large and different angular scales the first term in eq.(22) can make  $C^{G.s.n.}$  negative. When both angular scales are small the covariance is dominated by the intrinsic ellipticity noise (both upper panels with  $\theta_{si} < 2'$ ) but as soon as one scale is larger than  $10'$  the covariance is dominated by the cosmic variance (both upper panels with  $\theta_{si} > 2'$  and both lower panels for all  $\theta_{si}$ ). Then, except at large scales where  $\theta_{si} \sim \theta_{sj}$  the cosmic variance is dominated by the non-Gaussian terms which can be several orders of magnitude larger than the Gaussian contribution. Note that this is quite different from Fig. 4 which showed that non-Gaussian contributions were

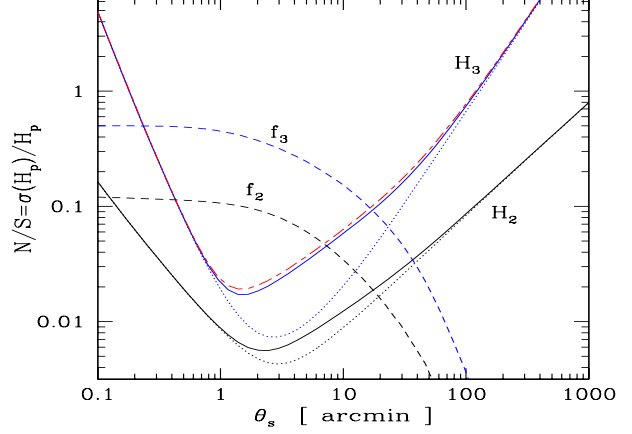


**Figure 9.** Inverse of the signal to noise ratios of the estimators  $\mathcal{H}_2$  and  $\mathcal{H}_3$  of the second-order and third-order cumulants of the aperture-mass. The solid lines show the ratios  $\sigma(H_p(i), H_p(i))/H_p(i)$  as a function of the angular scale  $\theta_{si}$  for  $p = 2$  (curve labeled  $\mathcal{H}_2$ ) and  $p = 3$  (curve labelled  $\mathcal{H}_3$ ) with no redshift binning. The covariance  $\sigma^2 = C_{ii}$  also corresponds to the solid line in Figs. 4-5. The dotted lines show the ratios obtained when we only include Gaussian terms in the covariance  $C_{ii}$  while the dashed lines correspond to the uncertainty associated with a 15% variation of  $f_2$  with respect to  $\mathcal{H}_2$  and a 50% variation of  $f_3$  with respect to  $\mathcal{H}_3$ . The dot-dashed line which follows closely the curve obtained for  $\mathcal{H}_3$  shows the noise/signal ratio when we use the estimator  $\mathcal{M}_3$  (eq.(11)) instead of  $\mathcal{H}_3$ .

not very important along the diagonal. Moreover, the non-Gaussian contribution to  $C_{ij}$  shows a broad plateau as we go farther from the diagonal. This feature, which makes the covariance matrix very broad about the diagonal and reflects a strong correlation between various angular scales, leads to difficulties for the estimation of cosmological parameters since the covariance matrix  $C_{ij}$  cannot be easily inverted.

The full covariance matrix along with its various components are shown in Fig. 7 for  $\mathcal{H}_2$ . In agreement with Figs. 4-6 the upper right panel which displays  $C^{G.s.n.}$  shows that the shot noise increases fastly at smaller angular scales. Its contribution to the covariance is restricted to the diagonal  $\theta_{s1} = \theta_{s2}$  above  $10'$  while it mostly depends on  $\max(\theta_{s1}, \theta_{s2})$  when both scales are below  $10'$ . On the other hand, the Gaussian contribution  $C^{G.v.}$  to the cosmic variance (lower right panel) is always restricted close to the diagonal and increases at large scales. The upper left panel which displays  $C^{c.v.}$  clearly shows that non-Gaussianities bring a significant broadening to the covariance matrix which is no longer diagonal-dominated. Finally, the lower left panel which displays the full covariance matrix  $C$  reflects these various factors and shows a very broad shape with a steep increase at small angular scales due to the shot-noise. Fig. 8 which shows the covariance matrix for  $\mathcal{H}_3$  exhibits a similar behaviour albeit with a stronger impact of non-Gaussianities.

## 5.2 Signal to noise ratios

Next, we plot in Fig. 9 the inverse  $N/S$  of the signal to noise ratios of the estimators  $\mathcal{H}_2$  and  $\mathcal{H}_3$  of the second-order and third-order cumulants of the aperture-mass. We show the ratios  $\sigma(H_p(i), H_p(i))/H_p(i)$  without redshift bin-



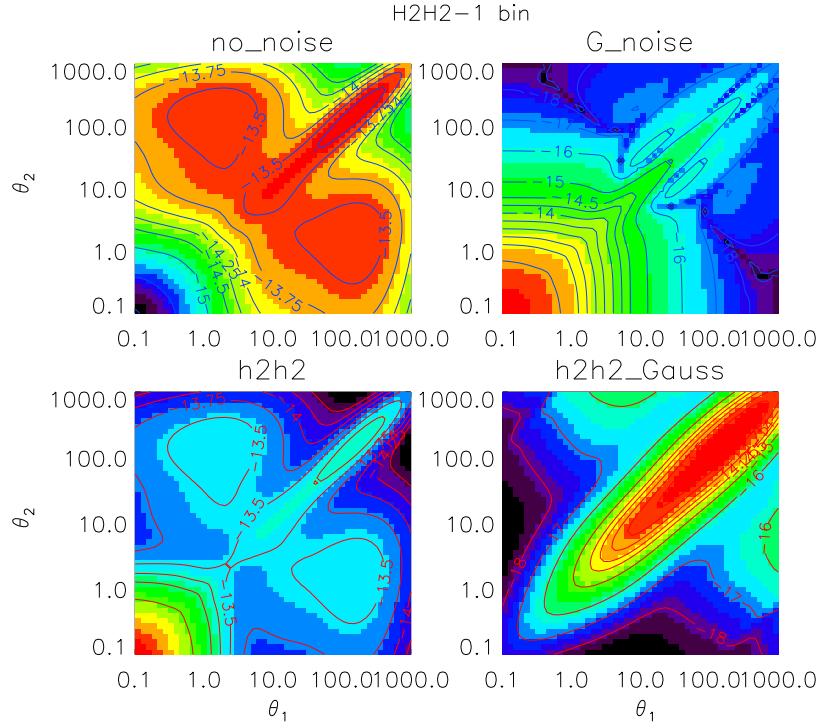


**Figure 7.** Covariance matrix for the estimator  $\mathcal{H}_2$  for different angular scales. We plot contours of constant  $\log C$ . *Lower left panel:* the full covariance  $C$ . *Upper left panel:* the cosmic variance contribution  $C^{c.v.}$  (i.e. the shot noise due to the galaxy intrinsic ellipticity dispersion is set to zero). *Lower right panel:* the Gaussian contribution  $C^{G,c.v.}$  to the cosmic variance. *Upper right panel:* the shot noise contribution  $C^{G,s.n.}$  to the Gaussian part of  $C$ .

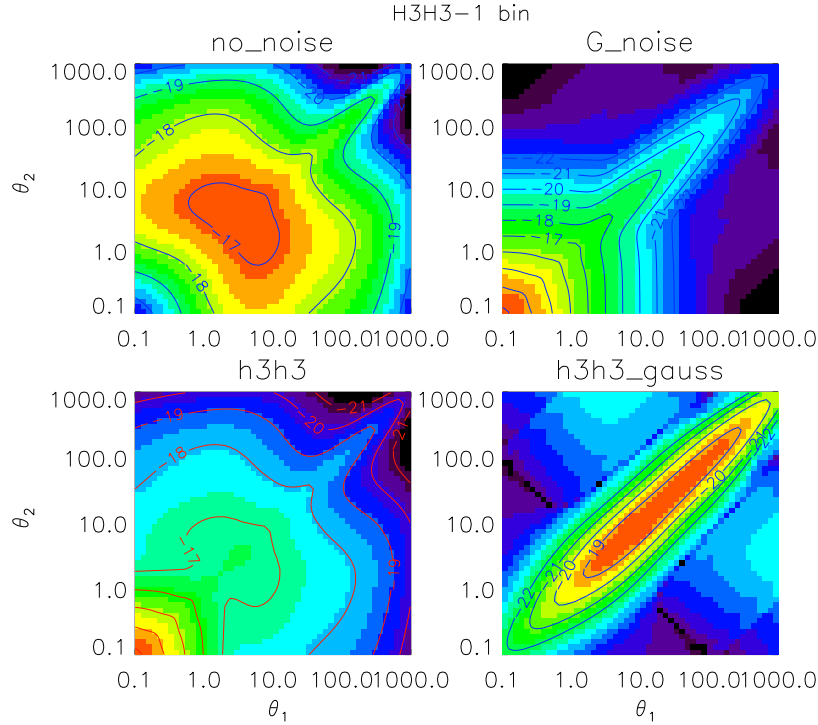


**Figure 8.** Same as previous figure but for the estimator  $\mathcal{H}_3$ . See text for discussion.

ning (solid lines). They grow at small scales because of the shot noise due to the galaxy intrinsic ellipticity dispersion and at large scales because of cosmic variance. We also display the noise to signal ratios  $N/S$  obtained when we only include the Gaussian terms  $C^G$  in the covariance  $C_{ii}$  (dotted lines). This corresponds to  $C^G = C^{G,s.n.} + C^{G,c.v.}$ , that is the sum of dotted lines and dashed lines shown in Figs. 4-5. In agreement with sect. 5.1 we find that non-Gaussian terms only make a difference in the intermediate range  $1' - 100'$  and that this effect is quite modest for the estimator  $\mathcal{H}_2$  of the variance  $\langle M_{ap}^2 \rangle$ . For  $\mathcal{H}_3$  the noise ratio can be increased by a factor 3 around  $3'$ . As discussed in sect. 5.1 non-Gaussian terms are mainly important for cross-correlations between different angular scales.

It is interesting to note that the angular scale at which the highest signal/noise ratio is achieved shifts to smaller angular scales when we include the contribution to cosmic variance from non-Gaussianities. Thus ignoring non-Gaussian terms in cosmic variance not only gives a wrong impression of higher signal to noise ratio, it also gives a wrong estimate of the angular scale where this is achieved. More detailed analysis of how these plots change with variations in survey characteristics are presented in the appendix, see fig. A1 and fig. A2. The very high S/N achieved by surveys such as SNAP for  $\mathcal{H}_3$  clearly indicates the potential of weak lensing surveys in studying even higher order non-Gaussianity such as  $\mathcal{H}_4$  which estimates the kurtosis of underlying mass distribution. The dot-dashed line which follows closely the curve obtained for  $\mathcal{H}_3$  shows the noise/signal ratio when we use the estimator  $\mathcal{M}_3$  (eq.(11)) instead of  $\mathcal{H}_3$ . Thus, in agreement with Valageas et al.(2005) we find that for third-order estimators there is not much gain to be obtained by switching from  $\mathcal{M}_3$  to  $\mathcal{H}_3$ . However, for higher-order non-Gaussianities like  $\mathcal{H}_4$  the improvement can be quite significant (see Figs.4 and 5 of Valageas et al. 2005).

Finally, the dashed lines in Fig. 9 show the noise associated with the current uncertainty on the non-linear regime of gravitational clustering, as described by the parameters  $f_2$  and  $f_3$ . Thus, the curve labeled  $f_2$  shows  $N/S = \Delta\mathcal{H}_2/\mathcal{H}_2$  with  $\Delta\mathcal{H}_2 = (\mathcal{H}_2(f_2 = 1.15) - \mathcal{H}_2(f_2 = 0.85))/2$  associated with a 15% variation of  $f_2$  as described in Fig. 1. In agreement with Fig. 1 and Fig. 9 this corresponds roughly to a 10% uncertainty on the non-linear power-spectrum. We can see that this is actually the dominant source of noise over the range  $0.2' - 20'$ . Next, the curve labelled  $f_3$  shows  $N/S = \Delta\mathcal{H}_3/\mathcal{H}_3$  with  $\Delta\mathcal{H}_3 = (\mathcal{H}_3(f_3 = 1.5) - \mathcal{H}_3(f_3 = 0.5))/2$  associated with a 50% variation of  $f_3$  as described in Fig. 2. In agreement with Fig. 2 and Fig. 9 this corresponds roughly to a 50% uncertainty on the non-linear skewness and third-order cumulant. This is the main source of noise over the range  $0.3' - 20'$ . Thus, in agreement with some previous studies we find that current theoretical uncertainties on non-linear gravitational clustering are the limiting factor to constrain cosmological parameters from large weak-lensing surveys with characteristics similar to the SNAP mission.

### 5.3 Cross-correlation of redshift bins

We show in Fig. 12 the noise/signal ratio we obtain for each redshift bin when we divide the sample into two sub-samples separated by the source redshift  $z_s = 1.23$ . The curves are similar to those displayed in Fig. 9 for the full sample. For

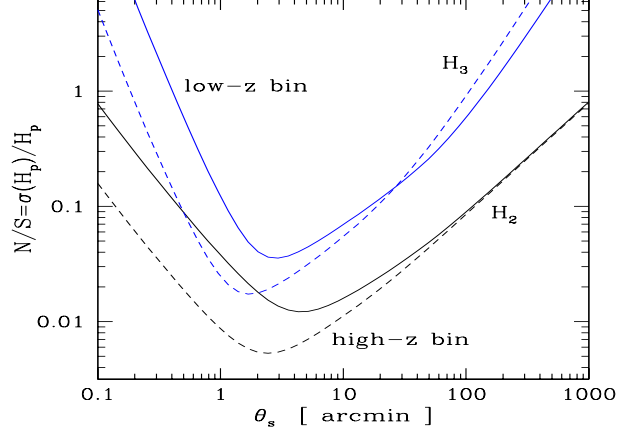


**Figure 12.** Inverse of the signal to noise ratios of the estimators  $\mathcal{H}_2$  and  $\mathcal{H}_3$  as in Fig. 9 but for two redshift bins. The solid lines correspond to the low redshift sub-sample ( $z_s < 1.23$ ) whereas the dashed lines show the results for the high redshift bin ( $z_s > 1.23$ ).

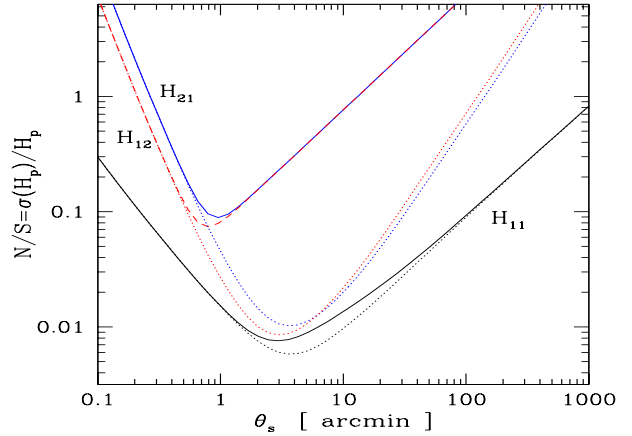


**Figure 13.** Inverse of the signal to noise ratios of the estimators  $\mathcal{H}_{11}$ ,  $\mathcal{H}_{21}$  and  $\mathcal{H}_{12}$  associated with the cross-correlation between both redshift bins. The solid lines are the full noise/signal ratios while the dotted lines are the results which we obtain when we only keep Gaussian terms in the covariance matrices.

clarity we do not show the curves associated with the theoretical uncertainties ( $f_2$  and  $f_3$ ) or with the Gaussian approximation to the covariance matrices. They also follow the behaviour of Fig. 9. We can see that the signal to noise ratio is larger for the high redshift bin (note that we plot its inverse  $N/S$ ). This is expected since the longer line of sight leads to a larger amplitude of weak lensing effects. However at very large angles the signal to noise ratio becomes slightly better for the low redshift bin for the estimator  $\mathcal{H}_3$  of non-Gaussianities because of the growth of non-Gaussian gravitational clustering.

Finally, we show in Fig. 13 the noise/signal ratios we obtain for the estimators  $\mathcal{H}_{11}$ ,  $\mathcal{H}_{21}$  and  $\mathcal{H}_{12}$  which directly measure the cross-correlation between both redshift bins. Here we defined  $\mathcal{H}_{pq}$  in a manner similar to  $\mathcal{H}_p$  introduced in sect. 2.2 such that their mean is:  $\langle \mathcal{H}_{pq} \rangle = \langle M_{ap1}^p M_{ap2}^q \rangle_c$  where  $M_{ap1}$  (resp.  $M_{ap2}$ ) is the aperture-mass associated with the low (resp. high) redshift bin, see Munshi & Valageas

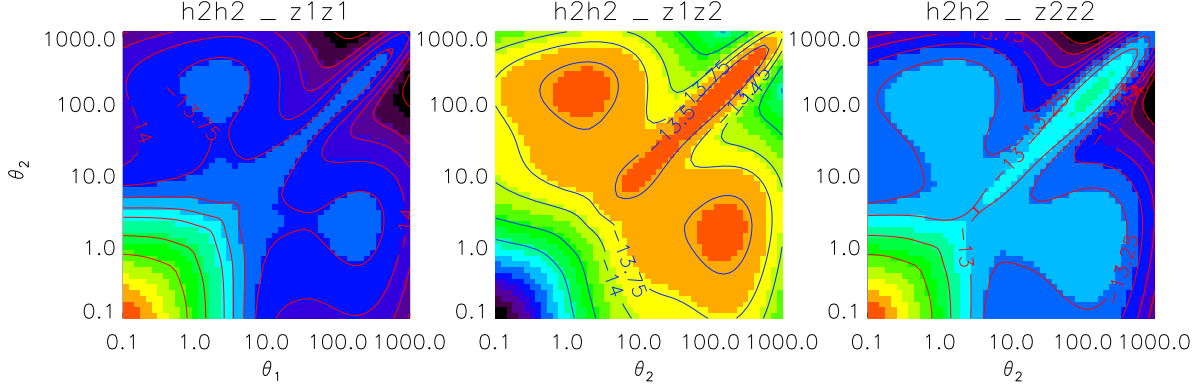


**Figure 10.** Covariance and cross-correlation is displayed for two different redshift bins. Left panel shows the covariance of  $\mathcal{H}_2$  for lower redshift bin and right panel corresponds to higher redshift bin. Middle panel shows the cross-correlation between both redshift bins.

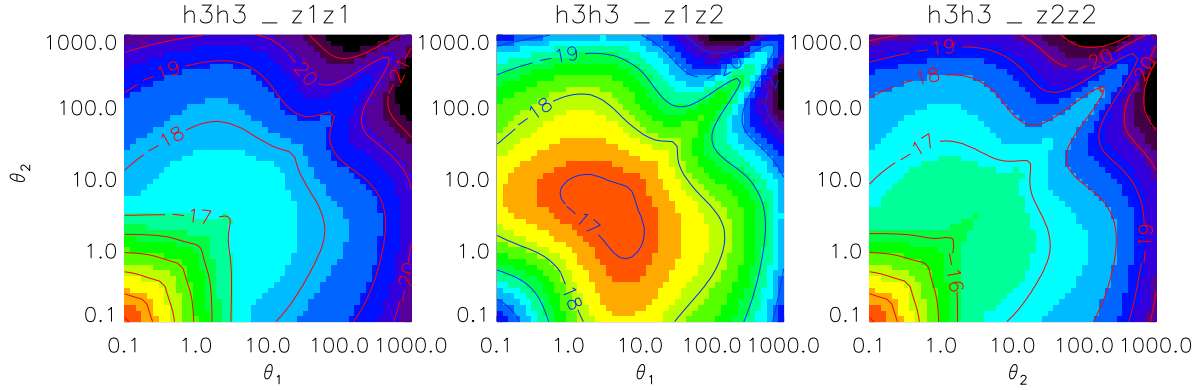


**Figure 11.** Same as Fig. 10 but for  $\mathcal{H}_3$ .

(2005). Of course we can check that the behaviour of different curves is similar to that obtained in previous figures. In particular, the signal to noise ratio is slightly better for  $\mathcal{H}_{12}$  than for  $\mathcal{H}_{21}$  since the former gives more weight to the high redshift bin, in agreement with Fig. 12. However, we note that the inclusion of non-Gaussian terms in the covariance matrices now makes a large difference for the third-order estimators  $\mathcal{H}_{21}$  and  $\mathcal{H}_{12}$ . Indeed, a Gaussian approximation could overestimate the signal to noise ratio by up to a factor ten.

The full covariance matrix is displayed in Fig. 10 for  $\mathcal{H}_2$  and Fig. 11 for  $\mathcal{H}_3$ . In agreement with the discussion above we find that the covariance is larger for the high-redshift bin, together with the weak lensing signal itself. As seen in Fig-12 the overall effect is still to improve the signal to noise ratio for the high- $z$  bin. The shape of the covariance matrix within each bin (left and right panels) is similar to the behaviour obtained for the full survey with no redshift binning (Figs. 7,8). The cross-correlation between both bins (middle panels) shows a similarly broad feature due to non-Gaussianities. However, there is no rise at small angular scales due to shot noise because there are no common galaxies to both bins (hence the shot noise contribution vanishes).

## 6 ESTIMATION OF COSMOLOGICAL PARAMETERS

### 6.1 Formalism

Baye's theorem (see e.g. Jaynes, 2003) provides an interesting starting point for most parameter estimation studies. Assuming a cosmological data vector  $\mathbf{a}$  the likelihood function of the cosmological parameter set  $\Theta$  can be described as:

$$\mathcal{L}(\Theta|\mathbf{a}) = \frac{\mathcal{L}(\mathbf{a}, \Theta)\mathcal{L}(\Theta)}{\mathcal{L}(\mathbf{a})}. \quad (32)$$

Here  $\mathcal{L}(\Theta)$  indicates the prior likelihood function of the parameter set  $\Theta$  and  $\mathcal{L}(\Theta|\mathbf{a})$  denotes the conditional likelihood function. Normalisation determines  $\mathcal{L}(\mathbf{a})$  and the prior comes from other cosmological observations or as in our case it is assumed to be constant as we do not include any other observational information. The factor  $\mathcal{L}(\mathbf{a}|\Theta)$  describes the distribution function of the observed data vector  $\mathbf{a}$  for a given cosmological parameter  $\Theta$ . Assuming a multi-variate Gaussian distribution one can express  $\mathcal{L}(\mathbf{a}|\Theta)$  as

$$\mathcal{L}(\mathbf{a}|\Theta) = \frac{1}{\sqrt{(2\pi)^N \det C(\Theta)}} \exp\left(-\frac{1}{2}\mathbf{a}^T \mathbf{C}^{-1}\mathbf{a}\right), \quad (33)$$

where  $\mathbf{C}^{-1}$  is the inverse of the covariance matrix  $\mathbf{C} = \langle \mathbf{a}^T \mathbf{a} \rangle - \langle \mathbf{a}^T \rangle \langle \mathbf{a} \rangle$  of the data vector  $\mathbf{a}$  being used. Associated log-likelihood statistic is defined as  $\chi^2/2$  where  $\chi^2 = \mathbf{a}^T \mathbf{C}^{-1} \mathbf{a}$ . The covariance matrix  $\mathbf{C}$  is a function of underlying cosmological parameters. Its derivatives w.r.t various cosmological parameters along with the derivatives of the mean  $\mu_\alpha$  are computed numerically while constructing the Fisher matrix  $F_{\alpha\beta}$ .

Assuming a fiducial cosmological model, for a given data vector, the estimation error of cosmological parameters associated with an unbiased estimator can be constructed from the Fisher matrix formalism (see Tegmark, 1997, Matsubara & Szalay 2002, Takada & Jain 2003). The Fisher information matrix (Kendall & Stuart 1969) which is related to the inverse covariance matrix for the cosmological parameter, assesses how well the data vector can distinguish the fiducial model from other models. Thus the error on the parameters  $\theta_\alpha$  obeys:  $\langle \Delta\theta_\alpha \Delta\theta_\beta \rangle \geq F_{\alpha\beta}^{-1}$ . The left hand side is computed for a specific values of the parameter vector  $\Theta_0$ . The equality is obtained for maximum likelihood estimates of the parameters. This inequality - which is also known as Cramér-Rao inequality - provides a minimum variance bound for unbiased estimators and can be used to study estimation error and their cross-correlation for various parameter sets for a given survey strategy. Analytical expression for the Fisher matrix  $F$  in terms of the covariance and mean of the data can be written as (Tegmark et al. 1997):

$$F_{\alpha\beta} = \mu_\alpha \mathbf{C}^{-1} \mu_\beta + \frac{1}{2} \text{Tr}[(\ln \mathbf{C})_\alpha (\ln \mathbf{C})_\beta] \quad (34)$$

where  $(\ln \mathbf{C})_\alpha = \mathbf{C}^{-1} \mathbf{C}_\alpha$  is the derivative of  $\ln \mathbf{C}$  w.r.t the parameter  $\theta_\alpha$ , and  $\mu_\alpha$  denotes the derivative of  $\mu = \langle \mathbf{a} \rangle$  w.r.t. the parameter  $\alpha$ .

The first term corresponds to the case when only mean is being estimated from the data vector whereas the second term is associated error for variance estimations from the data vector  $\mathbf{a}$ . The Fisher matrix is a positive-definite matrix. It is dominated by the linear order term related to estimation of mean of the data. With other cosmological data sets where the mean is fixed, such as mean temperature of the CMB, the variance term can be the dominant term. Here we include both terms in our analysis.

$$F_{\alpha\beta}(\Theta_0) = \left\langle \frac{\partial \ln \mathcal{L}(\mathbf{a}|\Theta)}{\partial \theta_\alpha} \frac{\partial \ln \mathcal{L}(\mathbf{a}|\Theta)}{\partial \theta_\beta} \right\rangle = - \left\langle \frac{\partial^2 \ln \mathcal{L}(\mathbf{a}|\Theta)}{\partial \theta_\alpha \partial \theta_\beta} \right\rangle \quad (35)$$

Where  $\langle \dots \rangle$  represents averaging over all possible data realization for fixed cosmological parameter values  $\Theta = \Theta_0$ . The equations of ellipsoid defined by the equation  $\sum_{\alpha,\beta} \Delta\theta_\alpha F_{\alpha\beta} \Delta\theta_\beta = \lambda^2$  define regions in a multidimensional parameter space which can be interpreted as error bounds for an experimental setup. A specific choice for  $\lambda$  defines a  $\lambda\sigma$  confidence level. Although strictly speaking such an interpretation is valid only when the likelihood function is Gaussian, for a mildly non-Gaussian case it can still provide a valuable idea about errors associated with estimators.

Therefore, up to a normalisation constant the marginalised two-dimensional likelihood function  $\mathcal{L}(\theta_\alpha, \theta_\beta)$  for two parameters  $\theta_\alpha$  and  $\theta_\beta$  can be expressed as:

$$\sim \exp \left[ -\frac{1}{2} (\Delta\theta_\alpha, \Delta\theta_\beta) \begin{pmatrix} F_{\alpha\alpha}^{-1} & F_{\alpha\beta}^{-1} \\ F_{\beta\alpha}^{-1} & F_{\beta\beta}^{-1} \end{pmatrix} \begin{pmatrix} \Delta\theta_\alpha \\ \Delta\theta_\beta \end{pmatrix} \right] \quad (36)$$

Here  $(F^{-1})_{\alpha\beta}$  represents the  $\alpha\beta$ -element of the inverse of the original higher dimensional Fisher matrix  $F$ . The marginalised error-ellipses therefore can be directly deduced from this expression. The likelihood contours start to deviate from their Fisher counterparts when higher-order correction terms start to become important at a large distance from the minima.

In general when a partial set of parameters is being marginalised over the other parameters the error covariance of the remaining parameters is given by a sub-matrix of the Full inverse Fisher matrix  $F^{-1}$ . Marginalisation in general causes a broadening of error ellipses due to reduced level of prior information being used.

$$F = \begin{pmatrix} F_{AA} & F_{AB} \\ F_{AB}^T & F_{BB} \end{pmatrix} \quad (37)$$

It can be shown that the marginalised  $n_A \times n_A$  Fisher matrix  $\tilde{F}$  can be expressed as  $\tilde{F} = F_{AA} - F_{BB} F_{CC}^{-1} F_{BB}^T$ . The second term in this expression provides the correction to the first term, due to marginalisation. In the absence of cross-correlations the correction term vanishes.

In our study, the data vector  $\mathbf{a}$  consists of various choices of measurements of  $\mathcal{H}_2$  and  $\mathcal{H}_3$  at different angular scales for different redshift bins  $\mathbf{a}_i = (\mathcal{H}_2(i; z_a), \mathcal{H}_3(i; z_a))$ . Here we have introduced additional index  $a$  for parametrising the redshift bin  $z_a$  under consideration. A slightly compact notation was used in previous sections where  $i$  was allowed to run over different angular scales and different redshift bins. Accordingly the Covariance matrix has a block structure with various blocks denoting covariance of  $\mathcal{H}_2(i; z_a)$  and  $\mathcal{H}_2(i; z_a)$  along with their cross-covariances between same and different redshift bins. In our analysis we have considered various combinations of the estimators  $\mathcal{H}_2$  and  $\mathcal{H}_3$  independently and jointly and for one or two redshift bins to study errors in parameter estimation. Different cases that we have considered can be summarised as below.

- Various angular scales  $\theta_s$  with *no* redshift information, and only 2-point information from  $\mathcal{H}_2(i)$ .
- Various angular scales  $\theta_s$  with *no* redshift information, but 2-point  $\mathcal{H}_2(i)$  and 3-point  $\mathcal{H}_3(i)$  information.
- Various angular scales  $\theta_s$  *with* redshift information, but only 2-point  $\mathcal{H}_2(i, z_a)$  information.
- Various angular scales  $\theta_s$  *with* redshift information, with both 2-point and 3-point  $\mathcal{H}_2(i, z_a), \mathcal{H}_3(i, z_a)$  information.

For each of these choices we analyse various combinations of cosmological parameters independently or jointly with or without a prior information regarding median source redshift  $z_0$ . Without prior redshift information the joint covariance matrix  $\mathbf{C}$  is ill-conditioned and numerical inversions are less stable. Due to broad covariance structure of the matrix  $\mathbf{C}$  there are no completely independent information at different angular scales  $\theta_{si}$ , especially when there is no redshift information.

## 6.2 Use of redshift binning and third-order estimators

In Figs. 14-17 we present our results from the Fisher analysis described in sect. 6.1 for various cosmological parameter pairs, combining the three angular scales  $\theta_s = 0.1', 10'$

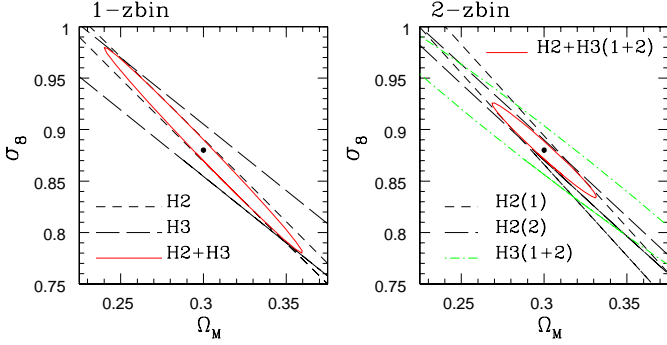


**Figure 14.** Results of Fisher matrix analysis for the parameter pair  $\{\Omega_m, \sigma_8\}$ , combining the three angular scales  $\theta_s = 0.1', 10'$  and  $1000'$ . Perfect knowledge of other parameters is assumed. For clarity only  $3\sigma$  contours are displayed. *Left panel:* Fisher ellipses obtained without redshift binning when we consider only the variance  $\langle M_{\text{ap}}^2 \rangle$  (estimator  $\mathcal{H}_2$ , dashed line), only the third order cumulant  $\langle M_{\text{ap}}^3 \rangle_c$  (estimator  $\mathcal{H}_3$ , long dashed line), and both cumulants for joint analysis ( $\mathcal{H}_2$  and  $\mathcal{H}_3$ , solid line). *Right panel:* Fisher analysis with two redshift bins. We consider the two bins separately for  $\mathcal{H}_2$  (dashed and long dashed lines) and jointly for  $\mathcal{H}_3$  only (dot-dashed line) and for the joint pair  $\mathcal{H}_2$  and  $\mathcal{H}_3$  (solid line).

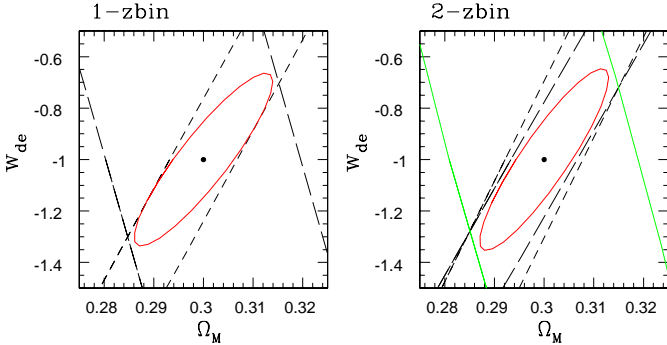


**Figure 15.** Same as Fig. 14 but for the  $\{\Omega_m, w_{\text{de}}\}$  pair.

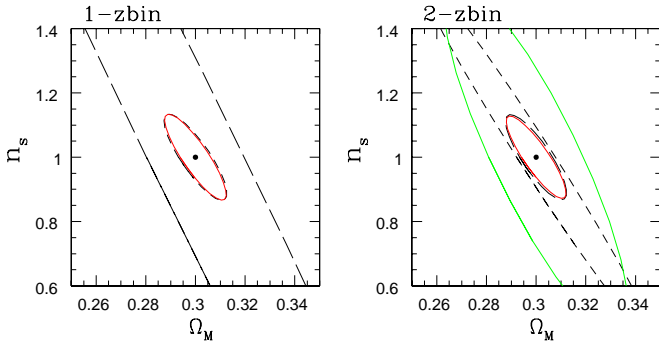


**Figure 16.** Same as Fig. 14 but for the  $\{\Omega_m, n_s\}$  pair.

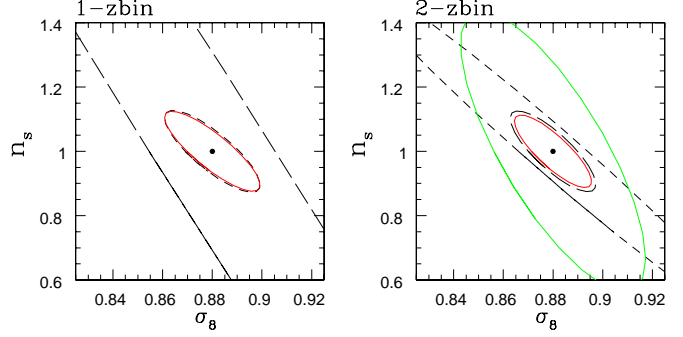


**Figure 17.** Same as Fig. 14 but for the  $\{\sigma_8, n_s\}$  pair.

and  $1000'$ . Perfect knowledge of remaining parameters is assumed in each case and only  $3\sigma$  contours are plotted for clarity. We display both separate and joint analysis of second-order and third-order cumulants (estimators  $\mathcal{H}_2$  and  $\mathcal{H}_3$ ) as well as the results obtained without redshift binning (left panels) and with two redshift bins (right panels). As expected, we find that in all cases the  $3\sigma$  contours are much larger for the third-order cumulant  $\langle M_{\text{ap}}^3 \rangle_c$  than for the variance  $\langle M_{\text{ap}}^2 \rangle_c$ . Higher-order cumulants would be even more noisy. However, for the pairs  $\{\Omega_m, \sigma_8\}$  and  $\{\Omega_m, w_{\text{de}}\}$  the degeneracy directions (long axis of the ellipse) are significantly different so that combining  $\mathcal{H}_2$  and  $\mathcal{H}_3$  greatly improves the constraints on cosmology as compared with  $\mathcal{H}_2$  alone (see left panels). Indeed, the long axis of the  $\mathcal{H}_2$ -ellipse can be fairly reduced by the intersection with the small axis of the  $\mathcal{H}_3$ -ellipse. This is most clearly seen in Fig. 15 for the  $\{\Omega_m, w_{\text{de}}\}$  pair. For the  $\{\Omega_m, n_s\}$  and  $\{\sigma_8, n_s\}$  pairs where the  $3\sigma$  ellipses associated with  $\mathcal{H}_2$  and  $\mathcal{H}_3$  are almost aligned the  $\mathcal{H}_2$  contour is well within the  $\mathcal{H}_3$ -ellipse so that adding the third-order cumulant does not tighten the constraints on cosmology.

Next, we show in the right panels the effects of redshift binning. For the  $\{\Omega_m, \sigma_8\}$  pair the  $\mathcal{H}_2$ -ellipses have a very high eccentricity and are very thin so that the small change of orientation between the two redshift bins leads to a significant tightening of the intersection area which improves the constraints on these cosmological parameters. For other pairs of parameters the  $\mathcal{H}_2$ -ellipses associated with the lower redshift bin (1) are significantly broader than for the high redshift bin and do not improve the constraints on cosmology. Then, redshift binning is not really useful in these cases. The fact that the low redshift bin yields poorer constraints on cosmological parameters can be understood from the smaller line of sight which gives less room for weak-lensing effects.

### 6.3 Comparison of Fisher analysis and $\chi^2$ likelihood

We now compare the results of the Fisher matrix analysis with the contour plots obtained through a  $\chi^2$  likelihood function. We again combine the three angular scales  $\theta_s = 0.1', 10'$  and  $1000'$  and we only display the joint analysis of second-order and third-order cumulants. We first show in Fig. 18 our results with no redshift binning. We can check

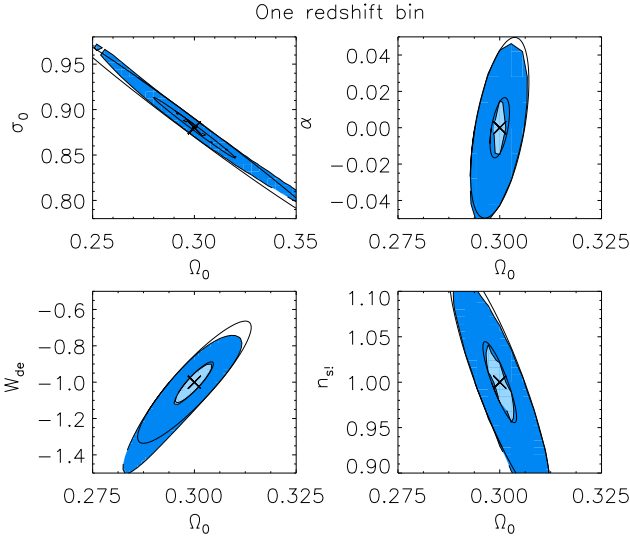


**Figure 18.**  $1\sigma$  and  $3\sigma$  Fisher ellipses compared with  $\chi^2$  contours, combining the three angular scales  $\theta_s = 0.1', 10'$  and  $1000'$  without redshift binning. We only display the results corresponding to joint analysis of second-order and third-order cumulants.

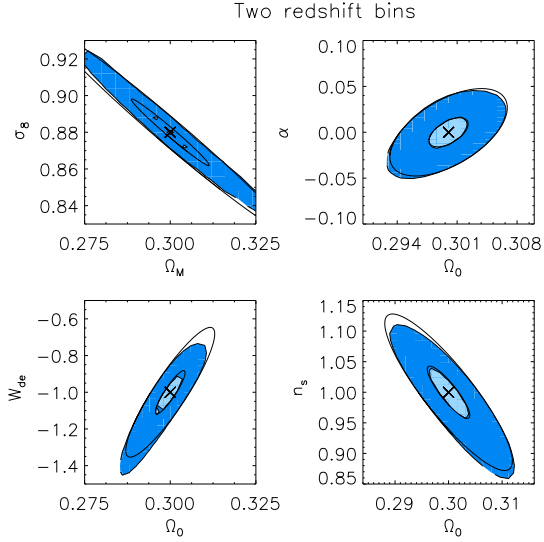


**Figure 19.** Same as Fig. 18 but using tomography. The survey is split into two redshift bins and their constraints on cosmology are combined to yield the contours shown in the four panels for various parameter pairs.

that the  $\chi^2$  likelihood agrees well with the Fisher matrix analysis. Moreover, it happens that both  $1\sigma$  and  $3\sigma$  contours are close to elliptic so that the Fisher matrix analysis appears to be sufficient, except for the broader  $3\sigma$  contour of the  $\{\Omega_m, w_{de}\}$  pair which is large enough to see distortions from the elliptic shape (i.e. far from the fiducial model  $\{\Omega_m = 0.3, w_{de} = -1\}$  the deviations of cumulants  $\langle M_{ap}^p \rangle_c$  are no longer linear). Next, we show in Figs. 19-20 a comparison of Fisher matrix analysis with the  $\chi^2$  likelihood func-

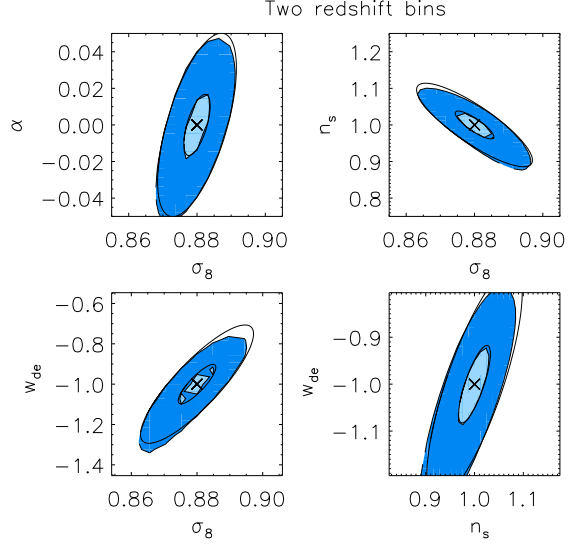


**Figure 20.** Same as Fig. 19 for other cosmological parameter pairs.

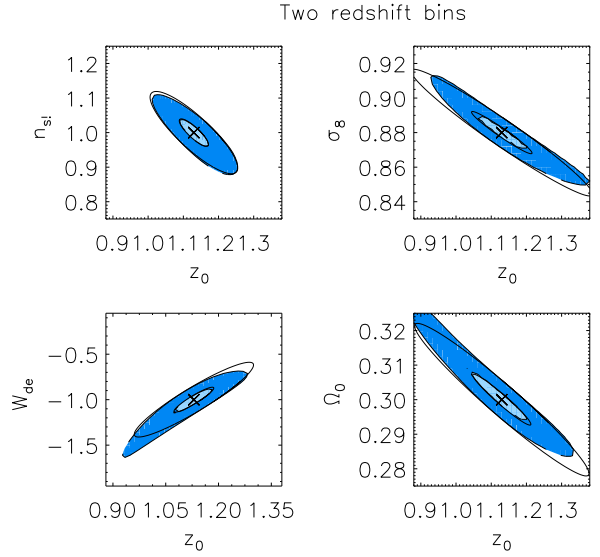


**Figure 21.** Same as Fig. 19 for other cosmological parameter pairs including the typical source redshift  $z_0$ .

tion using redshift binning. In agreement with sect. 6.2 we find that tomography is most efficient for the pair  $\{\Omega_m, \sigma_8\}$ . Both Fisher matrix and  $\chi^2$  contour plots are consistent, as in Fig. 18. Again, we find that the  $3\sigma$  areas are small enough to have elliptic shapes.

#### 6.4 Dependence on uncertainties on the mean redshift

We now investigate the impact of any uncertainty on the source redshift distribution onto weak-lensing results. Thus, we show in Fig. 21 Fisher matrix and  $\chi^2$  contours which can be obtained for various cosmological parameters letting the typical source redshift  $z_0$  defined in eq.(31) free (in each



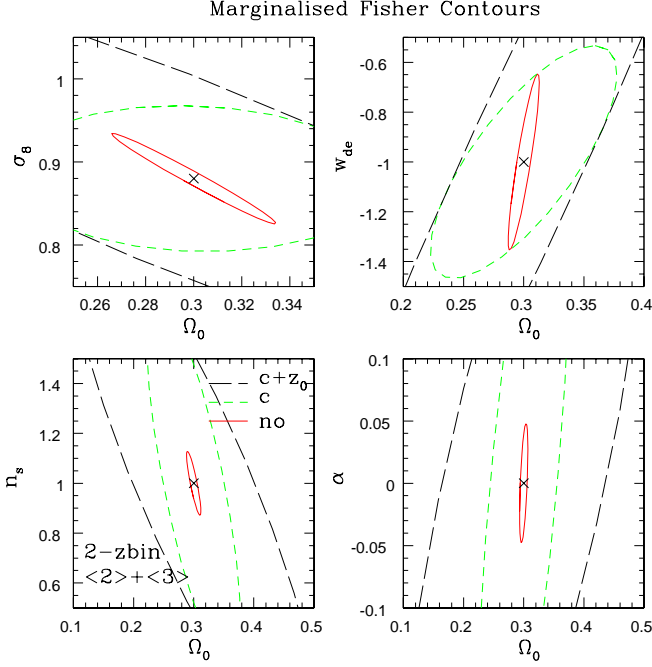


**Figure 22.** Marginalised 3- $\sigma$  Fisher contours are displayed for various pairs of cosmological parameters. The inner solid contours correspond to the case when all hidden parameters are assumed to be known perfectly. Outermost long-dashed lines correspond to the case when all hidden cosmological parameters and median redshift  $z_0$  are marginalised. The short-dashed line correspond to marginalisation of all hidden cosmological parameters except  $z_0$  (i.e. a perfect knowledge of  $z_0$  is assumed). In all cases two redshift bins are considered and information at the level of two-point and three-point are included for a SNAP class survey. Angular scales being considered are  $\theta_s = 0.1', 10'$  and  $1000'$ .

panel other parameters are assumed to be known). Then, we can directly read in Fig. 21 by how much any inaccuracy on the source redshift distribution can broaden the constraints on cosmology. Note that even when we do not impose any a priori on  $z_0$  such weak-lensing observations (assuming again that other parameters are given) are able to recover  $z_0$  by themselves up to 20%. If  $z_0$  is known to a better accuracy one can cut off the contours in Fig. 21. Depending on the cosmological parameter of interest we can see that the uncertainty on  $z_0$  can multiply the error bar on the former by a factor of 2 ( $n_s$ ) up to 4 ( $\Omega_m$  or  $\sigma_8$ ). Therefore, a good accuracy on the source redshifts can be quite rewarding.

### 6.5 Marginalizing over unknown parameters

Fig. 22 shows the individual error ellipses for parameter pairs as various degree of marginalisation is used. For the case of two redshift bins and joint analysis of 2-point and 3-point analysis we plot the effect of having no prior knowledge of  $z_0$  or any other parameters on estimation error. Clearly accurate knowledge of power-spectrum and bi-spectrum evolution is essential for putting any constraints on spectral index  $n_s$  or its run  $\alpha_s$ .

Results regarding marginalised errors are presented in units of  $f_{sky}^{-1/2}$  in table 1. Although the entries represent an extrapolation of flat-sky results to spherical sky, it is un-

likely that order of magnitudes are going to change with a more accurate all-sky approach. The second column shows  $F_{\alpha\alpha}^{-1/2}$  for individual parameters where complete knowledge of all other parameters is assumed. The third column shows marginalised errors when other parameters and  $z_0$  are unknown. Similarly the fourth column presents errors for additional prior of knowing only  $z_0$  perfectly. Last column corresponds to the determination of only  $\Omega_m$ ,  $\sigma_8$  and dark energy equation of state  $w_{de}$  whereas all other parameters are assumed to be known.

Finally, we present the cross-correlations  $r_{ij}$  among estimation errors for various parameter pairs in table 2. The significant correlations show that it is difficult to measure simultaneously all parameters with a good accuracy, if there are no priors from other data sets. This is consistent with Fig. 22 and with the comparison between the second and third columns of table 1.

## 7 DISCUSSION

We have used weak lensing tomography in real space at the level of two-point (equivalently power spectrum) and three-point (equivalently bi-spectrum) to study how accurately the background dynamics and the nature of dark energy can be probed from future weak lensing surveys such as SNAP. It is well known that the weight functions and the growth rate dependencies are different for the second  $\langle M_{ap}^2 \rangle$  and third-order  $\langle M_{ap}^3 \rangle$  moments. These complimentary information help to reduce the level of degeneracies along with the tomographical information in certain specific choices of cosmological parameters.

In our formalism, cross-correlation among various angular scales at different redshifts can be very easily incorporated in a natural way. Such a treatment is completely analytical and is an extension of previous study by Munshi & Coles (2002) which was later extended in Munshi & Valageas (2005). Assuming a “no-hole” approach it is possible to directly include all contributions to covariance matrices which include cosmic variance at large angular scales, shot noise at small angular scales and mixed terms at intermediate scales. Taking advantage of a complete analytical description, we have checked specific approximations to these covariances and their impact on error estimates of cosmological parameters. Over-enthusiastic simplifications of covariance structure of high-order estimators such as three-point estimators for  $\langle M_{ap}^3 \rangle$ , which depend increasingly on accurate description of non-Gaussianities, are typically absent in harmonic domain based approach and can lead to erroneous error-estimates.

Assuming a WMAP-centric  $\Lambda$ CDM cosmology, we have considered several cosmological parameters such as  $\Omega_m$ ,  $\sigma_8$ , spectral index  $n_s$ , running of spectral index  $\alpha_s$ , which determine the background dynamics of the universe, and the dark energy equation of state  $w_{de}$ .

Tomography in some cases can help to reduce the level of degeneracy in  $\{\sigma_8, \Omega_m\}$  or  $\{w_{de}, \Omega_m\}$  however interestingly in a large number of other cases most of the information seems to be coming only from the higher redshift bin and sub-dividing the sources in different redshift bins does not seem to affect the estimation accuracy. Equivalently while inclusion of higher order moments does indeed

**Table 1.** Scatter in estimated parameters in units of  $f_{\text{sky}}^{-1/2}$  for individual and joint estimation. Angular scales involved are  $0.1'$ ,  $10'$  and  $1000'$ . Values quoted within parenthesis are from two-point analysis whereas others are from joint analysis of two- and three-point statistics. Information from two redshift bins is considered. Different columns show the cases where we know all other parameters (2nd column), we marginalize over other cosmological parameters  $X_j$  and redshift  $z_0$  (3rd column), we marginalize over other parameters  $X_j$  only (4th column) and only the three parameters  $\{\Omega_m, \sigma_8, w_{\text{de}}\}$  are unknown.

$\langle M_{\text{ap}}^2 \rangle$	$F_{ii}^{-1/2}$	$[F^{-1}]_{ii}^{1/2} \{X_j, z_0\}$	$[F^{-1}]_{ii}^{1/2} \{X_j\}$	$[F^{-1}]_{ii}^{1/2} \{\Omega_m, \sigma_8, w_{\text{de}}\}$
$\sigma(\Omega_m)$	.00016(.00018)	.0059(.037)	.0022(.0039)	.0010(.0010)
$\sigma(\sigma_8)$	.00025(.00027)	.0075(.088)	.0025(.0160)	.0017(.0055)
$\sigma(w_{\text{de}})$	.00439(.00626)	.0606(.523)	.013(.4425)	.0116(.1357)
$\sigma(n_s)$	.00173(.00194)	.0305(.082)	.0207(.0258)	-
$\sigma(\alpha_s)$	.00111(.00112)	.0101(.011)	.0083(.0091)	-
$\sigma(z_0)$	.00181(.00204)	.0370(.405)	-	-

**Table 2.** Cross-correlation  $r_{ij}$  among estimation errors for various parameters. Values quoted within parenthesis are from two-point analysis whereas others are from joint analysis of two-point and three-point statistics. Two redshift bins are considered. Angular scales involved are  $0.1'$ ,  $10'$  and  $1000'$ .

$r_{ij}$	$\Omega_m$	$\sigma_8$	$w_{\text{de}}$	$n_s$	$\alpha_s$	$z_0$
$\Omega_m$	+1.00	-	-	-	-	-
$\sigma_8$	-0.88(-0.96)	+1.00	-	-	-	-
$w_{\text{de}}$	+0.96(+0.60)	-0.92(-0.37)	+1.00	-	-	-
$n_s$	-0.87(-0.97)	+0.56(+0.90)	-0.78(-0.63)	+1.00	-	-
$\alpha_s$	+0.75(+0.59)	-0.37(-0.53)	+0.64(+0.29)	-0.97(-0.75)	+1.00	-
$z_0$	+0.92(+0.99)	-0.94(-0.98)	+0.97(+0.53)	-0.73(-0.95)	+0.58(+0.55)	+1.00

help to break the parameter degeneracy for some parameter pairs, the other combinations are largely unaffected by inclusion of third order information. Clearly both tomography and non-Gaussianity information are more useful when a joint estimation of several parameters is performed. This is particularly true for spectral index  $n_s$  and its running  $\alpha_s$  which enter the modelling of bi-spectrum only through the description of power spectrum. Previous studies of tomography made use of Monte-Carlo simulations of correlated field of views (see e.g. Simon et al. 2004) across redshift bins. Our analytical results which do not rely on numerical simulations validate and generalise similar studies by including detailed descriptions of non-Gaussianities and cross-correlations among various redshift bins.

Generalised third order moments were considered recently by Kilbinger & Schneider (2005) which seem to be improving the situation by adding extra information at the level of third order. Interestingly however the highly correlated nature of such additional input suggests that one would only be restricted to a limited range of angular scales for construction of such a generalised quantities. A more general discussion of such generalised statistics which are also named as *cumulant correlators* in the literature can be found in Munshi & Valageas (2005). In our calculation here we have ignored the primordial non-Gaussianity which can potentially be studied at low redshift given the large sky-coverage of future weak lensing surveys. Recent results by Takada & Jain (2005) showed lensing fields do retain some information regarding primordial non-Gaussianity although it is expected that most of the information regarding baryon oscillations and primordial non-Gaussianities will be

erased by large scale non-linearities generated by gravitational clustering at a later epoch. Extension of our results in such directions to take into account additional cosmological parameters, with priors from external data sets such as Type-IA supernova or CMB observations, will be presented elsewhere. Additional parameters related to time evolution of dark energy equation of state or neutrino mass will also be included. Despite large sky-coverage even with future space based missions such as SNAP, error of estimation in various cosmological parameters remain inherently degenerate due to very nature of observables in weak lensing surveys. This is particularly underlined by the very high values of degradation factor  $(F_{\alpha\alpha})^{-1/2}/(F_{\alpha\alpha}^{-1})^{1/2}$  for various levels of marginalisation as presented in table-1. In table-2 scaled version of inverse Fisher matrix  $r_{\alpha\beta}$  which is also the cross correlation coefficient  $r_{\alpha\beta} = (F^{-1})_{\alpha\beta}/\{(F^{-1})_{\alpha\alpha}(F^{-1})_{\beta\beta}\}^{1/2}$  of estimation error of different parameters is plotted for certain choices of the parameters as indicated. Our findings are in agreement with a recent study by Kilbinger & Munshi (2005) where they reached a similar conclusion based on more elaborate generalised eigenmode analysis of Fisher matrices.

Knowledge of redshift distribution of source galaxies from external observations can help parameter estimation especially for smaller surveys. Even for larger surveys such as SNAP we found that order of magnitude improvement in accuracy is possible for almost all parameters we have studied. Large scale spectroscopy of a fair sample of faint source galaxies may not be possible, alternatively photometric redshift determination of subsample of observed galaxies can still improve the level of accuracy. It is likely that future ob-

servations with near complete sky coverage  $f_{sky} \sim 1$  spanning large redshift coverage can deal with much more detailed description of the source redshift distributions which we have only parametrised by one parameter  $z_0$ .

Several authors have recently studied joint constraints on various cosmological parameters such as  $\{n_s, \sigma_8\}$  and  $\{\alpha_s, n_s\}$  using Lyman-alpha forest data jointly with 1-year observations from WMAP (Spergel et al. 2003). Clearly the future space based SNAP class experiments will help to provide competitive constraints when used jointly with external data set.

Bi-spectrum of density fluctuations carries complementary information regarding background geometry and dynamics of the universe. Although current surveys are at the detection limit (see Bernardeau 2002) of measuring significant non-Gaussianity, it is expected that future space based observations with much greater sky coverage will supplement power spectrum information with accurate measurement of bi-spectrum. As we have shown here, this will require a very accurate description of evolution of bi-spectrum. Associating unknown parameters such as  $f_2$  and  $f_3$  with low order description of dark matter clustering and trying to estimate them directly from the data degrades the estimation accuracy of other cosmological parameters considerably.

Finally, in our studies we have compared Fisher analysis with full grid based  $\chi^2$  calculations. Importantly Fisher analysis should only be seen as a way to estimate minimum variance errors for unbiased estimators and to check degeneracy directions. It does not propose to reveal the detailed behaviour of the confidence plane far from the fiducial models. This is particularly true for very asymmetric constraints e.g. in  $(\Omega_m, \sigma_8)$  plane. Nevertheless the various parameter pairs that we have studied show a reasonable match in confidence level at  $1\sigma$  and even to  $3\sigma$  levels. An alternative approach which uses entropy functional to map out the likelihood distribution in the parameter space was considered in Taylor & Watts (2002). A grid based calculation of full  $\chi^2$  becomes prohibitively costly as the dimension of the parameter space increase. A more effective sampling of the parameter space can be achieved by Monte Carlo based Markov-Chain algorithms. A full implementation will be presented elsewhere.

In our present analysis we have focused on survey parameters similar to proposed SANP-class surveys (JDEM). It is not difficult to extend it to other survey specifications. With future well optimised surveys with large sky coverage, CFHTLS (172 deg<sup>2</sup>), SNAP (300 deg<sup>2</sup>), VISTA (10000 deg<sup>2</sup>), Pan-starr (31000 deg<sup>2</sup>) and recent data analysis techniques, weak lensing will be a very useful tool to probe not only standard cosmological parameters, such as  $\Omega_m$  and  $\sigma_8$ , but also the dark energy equation of state parameters such as  $w_{de}$ . However to achieve this goal it is essential to have a tight handle on systematics which should at least stay comparable to statistical errors.

## ACKNOWLEDGMENTS

DM was supported by PPARC of grant RG28936. It is a pleasure for DM to acknowledge many fruitful discussions with members of Cambridge Planck Analysis Center (CPAC). DM also thanks Martin Kilbinger, Alan Heavens,

Yun Wang, Lindsay King and George Efstathiou for useful discussions.

## REFERENCES

- Abazajian K., Dodelson S., 2002, Phys.Rev. D66, 023526
- Bacon D., Réfrégier A., Ellis R.S., 2000, MNRAS, 318, 625
- Bartelmann M., Schneider P., 2001, Phys. Rep., 340, 291
- Bardeen J.M., Bond J.R., Kaiser N., Szalay A.S., 1986, ApJ, 304, 15
- Benabed K., van Waerbeke L., 2004, Phys. Rev. D, 70, 123515
- Bernardeau F., van Waerbeke L., Mellier Y., 1997, A&A, 322, 1
- Bernardeau F., Mellier Y., 2002, A&A, 389, L28
- Contaldi C.R., Hoekstra H., Lewis A., 2003, Phys. Rev. Lett., 90, 221303
- Croft R.A.C., Metzler C.A., 2001, ApJ, 546, 561
- Crittenden R., Natarajan P., Pen U.-L., Theuns T., 2001, ApJ, 559, 552
- Eisenstein D.J., Hu W., 1999, ApJ, 511, 5
- Hamilton A.J.S., Tegmark M., Padmanabhan N., 2000, MNRAS, 317, L23
- Hamana T., Miyazaki S., Shimasaku K., Furusawa H., Doi M., et al., 2003, Ap.J., 597, 98
- Hämmerle H., Miralles J.M., Schneider P., Erben T., Fosbury R.A., 2002, A&A, 385, 743
- Heavens A., 2003, MNRAS, 343, 1327
- Heymans C., Brown M., Heavens A., Meisenheimer K., Taylor A., Wolf C., 2004, MNRAS, 347, 895
- Hoffmann Y., Zaroubi S., 2000, ApJ, 535, L5
- Hoekstra H., Yee H.K.C., Gladders M., 2002, ApJ., 577, 595
- Hu W., 1999, ApJ, 522, L21
- Hu W., Tegmark M., 1999, ApJL, 514, L65
- Huterer D., White M., 2005, submitted to PRD, also astro-ph/0501451
- Ishak M., Hirata C., McDonald P., Seljak U., 2004, PRD, 69, 083514
- Jarvis M., Bernstein G.M., Fisher P., Smith D., Jain B., Tyson J.A., Wittman D., 2002, ApJ, 125, 1014
- Jain B., Seljak U., 1997, 484, 560
- Jain B., Taylor A., PRL, 2003, 91, 141302
- Jaynes E.T., Probability Theory: The logic of Science, Cambridge University Press.
- Kaiser N., 1992, ApJ, 388, 272
- Kaiser N., 1995, ApJ, 439, L1
- Kaiser N., Wilson G., Luppino G.A., 2000, astro-ph/0003338
- Kaiser N., Wilson G., Luppino G., 2000, ApJ, 537, 555
- Karhunen H., 1947, Ann. Acad. Sci. Fennicae Ser. A.I. 37
- Kendall M.G., Stuart A., 1969, The Advanced Theory of Statistics, Vol. II (London:Griffin)
- Kilbinger M., Schneider P., 2004, A&A, 413, 465
- Kilbinger M., Munshi D., 2005, MNRAS, submitted, astro-ph/0509548
- Linder E.V., Jenkins A., 2003, MNRAS, 346, 573
- Loève M., 1948, Processes Stochastiques et Mouvement Brownien, (Hermann, Paris France)
- Maoli R., van Waerbeke L., Mellier Y., Schneider P., Jain B., Bernardeau F., Erben T., Fort B., 2001, A&A, 368, 766
- Matsubara T., Szalay A.S., Landy S.D., 2000 ApJ, 535, L1
- Mellier Y., 1999, ARA&A, 37, 127
- Munshi D., Coles P., 2003, MNRAS, 338, 846
- Munshi D., Valageas P., 2005, MNRAS, 356, 439
- Munshi D., Valageas P. To appear in 2005 Triennial Issue of Phil. Trans. A, astro-ph/0509216
- Peacock J.A., Dodds S.J., 1996, MNRAS, 280, L19
- Réfrégier A., Rhodes J., Groth E.J., 2002, ApJ, 572, L131
- Réfrégier, A. 2003, ARA&A, 41, 645
- Réfrégier, A. et al., (2004), Astron.J. 127, 3102

- Rhodes et al. 2003, (2004), *Astropart.Phys.* 20, 377  
 Schneider P. 1996, *MNRAS*, 283, 837  
 Schneider P., Lombardi, M., 2003, *A&A*, 397, 809  
 Schneider P., van Waerbeke L., Jain B., Kruse G. 1998, *MNRAS*, 296, 873  
 Schneider P., van Waerbeke L., Kilbinger M., Mellier Y., 2002, *A&A*, 396, 1  
 Schneider P., van Waerbeke L., Mellier Y., 2002, 398, 729  
 Kilbinger P., Schneider P., 2005, To appear in *A&A*, astro-ph/0505581  
 Kilbinger P., Schneider P. 2004, *A&A*, 413, 465  
 Simon P., King L.J., Schneider P., 2004, *A&A*, 417, 873  
 Scoccimarro R., Zaldarriaga M., Hui L. 1999, *ApJ*, 527, 1  
 Silberman L., Dekel A., Eldar A., Zehavi, I., 2001, *ApJ*, 557, 102  
 Smail I., Hogg D.W., Yan L., Cohen, J.G., 1995, *ApJ*, 449, L105  
 Spergel D.N., Verde L., Peiris H.V., et al., 2003, *ApJS*, 148, 175  
 Szalay A.S. et al., 2003, *ApJ*, 591, 1  
 Takada M., Jain B., *MNRAS*, 2004, 384, 897  
 Taylor A., Watts P., 2001, *MNRAS*, 328, 1027  
 Tegmark M., Taylor A., Heavens A., 1997, *ApJ*, 480, 22 (TTH)  
 Tereno I., Doré O., van Waerbeke L., Mellier Y., 2005, *A&A*, 429, 383  
 Tyson et al. (2002) in *Proc. 5th International UCLA Symposium on Sources and Detection of Dark Matter*, Marina del Rey, February 2002, ed. D. Cline  
 Valageas P., Munshi D., Barber A.J., 2005, *MNRAS*, 356, 386  
 van Waerbeke L., Bernardeau F., Benabed K., 2000, *ApJ*, 540, 14  
 van Waerbeke L. et al., 2000, 358, 30  
 van Waerbeke L., Mellier Y., Radovich M., et al., 2001, *A&A*, 374, 757  
 van Waerbeke L., Mellier Y., Pelló R., Pen U.-L., McCracken H.J., Jain B., 2002, *A&A*, 393, 369  
 van Waerbeke L., Mellier Y., 2003, in Valls-Gabaud D., Kneib J.P., eds., *ASP Conf. Ser., Gravitational lensing: A unique tool for cosmology*  
 van Waerbeke L., Mellier Y., Hoekstra H., 2005, *A&A*, 429, 75  
 van Waerbeke L., Mellier Y., Pelló R., Pen U.-L., McCracken H.J., Jain B., 2002, 393, 369  
 Wittman D.M., Tyson J.A., Kirkman D., Dell'Antonio I., Bernstein G., 2000, *Nature*, 405, 143  
 Vogeley M.S., Szalay A.S., 1996, *ApJ*, 465, 34  
 Watkins R., Feldman H.A., Chambers S.W., Gorman, P., Melott, A.L., 2002, *ApJ*, 564, 534

## APPENDIX A: OTHER SURVEY CHARACTERISTICS

For completeness, we display in this appendix the noise to signal ratios we obtain for different survey properties. Thus, we display in Fig. A1 our results for the SNAP survey as in Fig. 9 (solid lines) as well as for the cases when we divide by a factor two its area (dashed line), its galaxy number density (dotted lines) or its depth (dot-dashed lines). When the depth of the survey is varied the dashed curves labeled  $f_2$  and  $f_3$  change slightly (as the redshift distribution of sources whence of the density fluctuations probed by the survey is varied) but since the modification is very small (by definition the curves show the same plateau at small scales) we do not add them in Fig. A1 for clarity. We can check that a smaller galaxy number density increases the noise at small scales (below  $2'$ ) which is dominated by shot noise but does not change the signal to noise ratio at large scales which is governed by the cosmic variance. By contrast, a smaller area leads as expected to a smaller signal to noise ratio at all scales. Finally, a smaller depth decreases the signal to noise

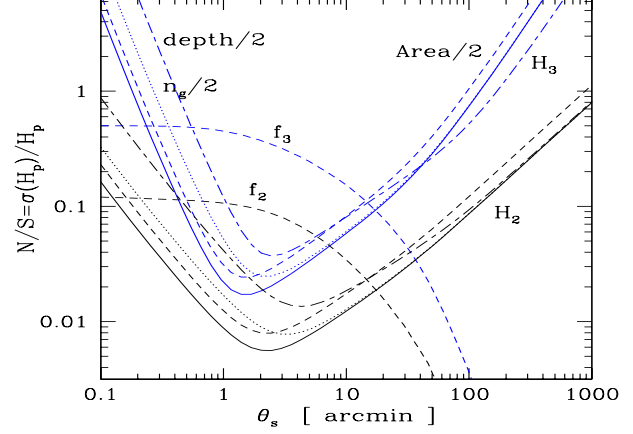


**Figure A1.** Inverse of the signal to noise ratios of the estimators  $\mathcal{H}_2$  and  $\mathcal{H}_3$  of the second-order and third-order cumulants of the aperture-mass for various survey properties. The solid lines correspond to the SNAP survey as in Fig. 9, the dashed lines to a similar survey with an area twice smaller ( $A = 150 \text{ deg}^2$ ), the dotted lines to a galaxy number density twice smaller ( $n_g = 50 \text{ arcmin}^{-2}$ ) and the dot-dashed lines to a survey with a depth which is twice smaller ( $z_0 = 0.57$  and  $z_{\text{max}} = 1.5$ ). There is no redshift binning and we use the full covariance  $C_{ii}$ .

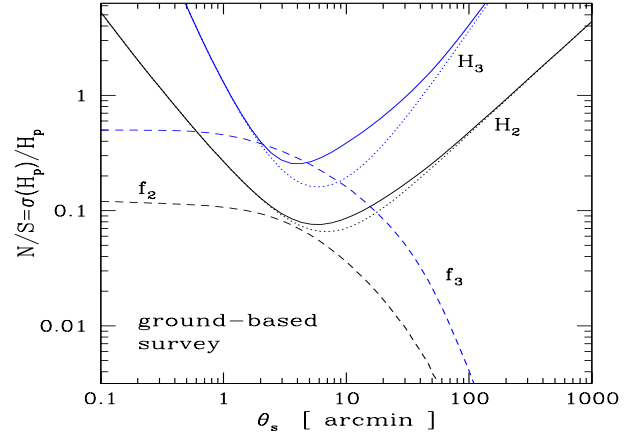


**Figure A2.** Inverse of the signal to noise ratios of the estimators  $\mathcal{H}_2$  and  $\mathcal{H}_3$  of the second-order and third-order cumulants of the aperture-mass as in Fig. 9 but for a typical ground-based survey. There is no redshift binning. The solid lines correspond to the full covariance  $C$  while the dotted line shows the results we obtain when we only use its Gaussian part  $C^G$ .

ratio at small scales as the amplitude of gravitational lensing effects is weaker because of the smaller line of sight while the shot noise remains the same. At large scales the signal to noise ratio for  $\mathcal{H}_2$  is not diminished while it improves somewhat for  $\mathcal{H}_3$  (at fixed galaxy number density) as the survey focuses more on the non-linear regime of gravitational clustering where non-Gaussianities are larger.

Next, we show in Fig. A2 the noise to signal ratios obtained for a typical ground-based survey with a galaxy distribution  $n(z_s) \propto z_s^2 e^{-(z_s/0.8)^{1.5}}$ , an area  $A = 10 \text{ deg}^2$  and a galaxy number density  $n_g = 20 \text{ arcmin}^{-2}$  (e.g., van Waerbeke et al. (2001)). Of course, we can check that both the

shot-noise and the cosmic variance are significantly larger than for a space-based mission such as SNAP. This implies that the range of scales which can be used to extract cosmological information is quite smaller. On the other hand, the theoretical uncertainty on the non-linear regime of gravitational clustering (denoted by the dashed curves) is only of the same order as other sources of noise around  $5'$  and is relatively smaller at other scales, so that it is not really the limiting factor for such surveys.

A generalised eigen mode analysis (Loève 1948, Karhunen 1947) which can address the issue of optimisation of survey design  $(z_0, f_{sky}, n_g)$  for recovery of a given set of cosmological parameters in line with Kilbinger & Munshi (2005) but including tomography and non-Gaussianity will be presented elsewhere.